

**MODELING OF D/C MOTOR DRIVEN SYNTHETIC JET
ACTUATORS FOR FLOW SEPARATION CONTROL**

A Thesis

by

ASHWIN KUMAR BALASUBRAMANIAN

Submitted to the Office of Graduate Studies of
Texas A&M University
in partial fulfillment of the requirements for the degree of

MASTER OF SCIENCE

August 2003

Major Subject: Aerospace Engineering

**MODELING OF D/C MOTOR DRIVEN SYNTHETIC JET
ACTUATORS FOR FLOW SEPARATION CONTROL**

A Thesis

by

ASHWIN KUMAR BALASUBRAMANIAN

Submitted to Texas A&M University
in partial fulfillment of the requirements
for the degree of

MASTER OF SCIENCE

Approved as to style and content by:

Othon K. Rediniotis
(Chair of Committee)

James G. Boyd
(Member)

Mark T. Holtzapple
(Member)

Ramesh Talreja
(Department Head)

August 2003

Major Subject: Aerospace Engineering

ABSTRACT

Modeling of D/C Motor Driven Synthetic Jet Actuators for Flow Separation Control.

(August 2003)

Ashwin Kumar Balasubramanian, B.Tech., Indian Institute of Technology, Chennai,
India

Chair of Advisory Committee: Dr. Othon K. Rediniotis

The objective of this research is to present a theoretical study of the compressibility effects on the performance of an electric D/C motor driven synthetic jet actuator for flow separation control. Hot wire anemometer experiments were conducted to validate the jet exit velocities predicted by the theoretical model. The optimal jet exit velocity required to achieve maximum flow reattachment at reasonable blowing momentum coefficients(C_{μ}) is predicted. A dynamic electro-acoustic model of the D/C motor driven actuator is developed to accurately predict its performance and efficiency. This model should help formulate a feedback optimal control strategy for real-time flow control using an array of actuators. This model is validated by comparing it with hot wire anemometer experiments conducted under similar conditions. The effects of geometric parameters like the slot width, slot geometry, and cavity volume on the performance of the actuator are also tested using this model.

DEDICATION

I dedicate my work in its entirety to my parents, the late Professor S. Balasubramanian and Mrs. Lalitha Balasubramanian. The encouragement and motivation provided by them is beyond any words of description.

ACKNOWLEDGEMENTS

I am very grateful to my advisor, Dr. Othon K. Rediniotis whose invaluable guidance and support has helped me perform to the best of my ability throughout my career as a graduate student. I would also like to thank Mr. Rick Allen at the machine shop for his invaluable help in setting up all my experiments. I am also indebted to all my friends for their support in my efforts.

TABLE OF CONTENTS

	Page
ABSTRACT	iii
DEDICATION	iv
ACKNOWLEDGEMENTS	v
TABLE OF CONTENTS	vi
LIST OF FIGURES	viii
LIST OF TABLES	xi
NOMENCLATURE	xii
INTRODUCTION	1
EXPERIMENTAL FACILITIES	7
Hot wire anemometry	7
Software	8
STUDY OF COMPRESSIBILITY EFFECTS OF DC MOTOR DRIVEN SJAs	9
Introduction	9
THEORETICAL MODEL TO PREDICT COMPRESSIBILITY EFFECTS	11
Model without accounting for friction losses at exit	11
Results and discussion	15
Model accounting for friction losses and separation effects at exit	27
Determining the constant, c	29
Results and discussion	29
Experimental studies using hot wire anemometry	36
Results and discussion of experimental study	37
Conclusions	46
ELECTRO-ACOUSTIC MODEL OF D/C MOTOR DRIVEN SJA	47
Introduction	47
Physical representation of electro-acoustic circuit	48
Evaluation of frequency response function	51
Determination of impedances in circuit	58

	Page
Piston terms	58
Cavity terms	63
Neck / Exit slot terms	63
Results and discussion of effects of geometric parameters on electro-acoustic model	67
Order of magnitude analysis for the impedances	67
Conclusions	78
CONCLUSIONS	80
REFERENCES	81
APPENDIX A	84
APPENDIX B	86
APPENDIX C	89
VITA.....	96

LIST OF FIGURES

	Page
FIGURE 1. General schematic of a synthetic jet actuator.	11
FIGURE 2. Design of SJA exit slot / cavity.	16
FIGURE 3. Design of exit slot plate.	16
FIGURE 4. Jet exit velocity comparison for incompressible and compressible flow. ...	17
FIGURE 5. Exit velocity comparison between compressible and incompressible flow for different acceleration lengths.....	18
FIGURE 6. Variation of jet exit velocity with cavity volume for slot width 0.032”.....	20
FIGURE 7. Variation of jet exit velocity with cavity volume for slot width 0.064”.....	21
FIGURE 8. Variation of maximum and minimum pressure at the center of the cavity.	22
FIGURE 9. Jet exit velocity comparison between compressible and incompressible case for six-cylinders SJA.	24
FIGURE 10. Variation of exit velocity with 10, 20 and 30 % increase in cavity volume for six-cylinders SJA.	25
FIGURE 11. Variation of jet exit velocity with 10, 20 and 30 % decrease in cavity volume for six-cylinders SJA.	26
FIGURE 12. Maximum and minimum pressure at center of cavity.	27
FIGURE 13. Jet exit velocity comparison between incompressible and compressible cases with and without friction losses for slot width 0.032”.....	30
FIGURE 14. Jet exit velocity comparison between incompressible and compressible cases with and without friction losses for slot width 0.064”.....	31
FIGURE 15. Variation of jet exit velocity with slot width for the compressible case accounting for friction losses at exit.....	32
FIGURE 16. Variation of jet exit velocity with cavity volume for the compressible case with and without friction for slot width 0.032”.....	34
FIGURE 17. Variation of jet exit velocity with cavity volume for the compressible case with and without friction losses for slot width 0.064”.....	35

	Page
FIGURE 18. Jet exit velocity comparison between experiment and theoretical compressible case without accounting for friction losses at slot width 0.032”	38
FIGURE 19. Jet exit velocity comparison between experiment and theoretical compressible case without accounting for friction losses at slot width 0.064”	39
FIGURE 20. Jet exit velocity comparison between experimental and theoretical compressible cases with and without accounting for friction losses at exit for slot width 0.032”	40
FIGURE 21. Jet exit velocity comparison between experimental and theoretical compressible cases with and without accounting for friction losses at exit for slot width 0.064”	41
FIGURE 22. Variation of jet exit velocity with slot width for experimental study and the theoretical compressible model accounting for friction losses.....	42
FIGURE 23. Variation of exit velocity with cavity volume for the experimental study and the theoretical compressible model accounting for friction losses for slot width 0.032”	44
FIGURE 24. Variation of exit velocity with cavity volume for experimental study and theoretical compressible model accounting for friction for slot width 0.064”	45
FIGURE 25. Crankshaft disk design.....	53
FIGURE 26. Crankshaft end design.....	54
FIGURE 27. Crankshaft section design.....	54
FIGURE 28. Connecting rod design.....	55
FIGURE 29. Electro-acoustic model circuit of DC motor driven SJA.....	56
FIGURE 30. Box circuit of the electro-acoustic model of DC motor driven SJA.....	57
FIGURE 31. Frequency dependence of acoustic mass of air moving the piston.....	68

	Page
FIGURE 32. Frequency dependence of the acoustic resistance of mechanical parts moving with piston.	69
FIGURE 33. Frequency dependence of the acoustic resistance of air moving with piston.....	70
FIGURE 34. Frequency dependence of the acoustic mass of air in exit neck.	71
FIGURE 35. Frequency dependence of the viscous resistance of air in the exit neck.....	72
FIGURE 36. Comparison between electro-acoustic model and incompressible and compressible theoretical models at slot width 0.032".	73
FIGURE 37. Comparison between electro-acoustic model and incompressible and compressible theoretical models at slot width 0.064".	74
FIGURE 38. Compressibility prediction using electro-acoustic model for both large and small slot.	75
FIGURE 39. Variation of exit velocity with slot width using electro-acoustic model. ...	76
FIGURE 40. Comparison between electro-acoustic model prediction and experimental studies for slot width 0.032".	77
FIGURE 41. Comparison between electro-acoustic model prediction and experimental studies at 0.064" slot width.....	78

LIST OF TABLES

	Page
TABLE 1. Software used in thesis.....	8
TABLE 2. Different geometric parameters of SJAs tested for compressibility effects...15	15
TABLE 3. Geometric parameters of six cylinders SJA tested with model.....23	23
TABLE 4. Characteristics of Astro Cobalt Marine Racing D/C motor driving the SJA. 52	52
TABLE 5. Different geometric parameters of SJA tested using electro-acoustic model.67	67

NOMENCLATURE

$F+$	Design forcing frequency of actuator
C_μ	Oscillatory blowing momentum coefficient
R_E	Reynolds Number
M	Mach number
C	Airfoil chord
x	Displacement of piston
\dot{x}	Velocity of piston
V_o	Volume of cavity + cylinder when $x=0$
p_d	Piston diameter
ccl	Cylinder cavity length
A_P	Area of piston
S_W	Exit slot width
S_L	Exit slot length
A_S	Area of exit slot
l	Acceleration length of air in the exit slot
ρ	Density of air
U	Amplitude of jet exit velocity
U_∞	Free stream velocity of air
X_∞	Any free stream quantity
dm/dt	Mass flow rate of air in the system
f	Frequency of oscillation of motor
M_P	Mass of piston and other moving mechanical parts
A	Amplitude of piston displacement
P_S	Stroke of the piston
ϕ	Velocity potential
p	Pressure of air
p_o	Atmospheric pressure
p_c	Pressure of air at the center of the cavity

L_E	Acceleration length of air in the exit slot / Equivalent inertia length of the slot
T	Ambient temperature
T_o	Standard atmospheric temperature
R	Universal gas constant
μ	Dynamic viscosity of air
ν	Kinematic viscosity of air
L_V	Equivalent viscous length of exit slot
C_D	Flow coefficient associated with streamline curvature at exit plane of slot
L_T	Geometric length of exit slot
h_T	Resonator throat height
H_C	Height of cavity
L_C	Length of cavity
W_C	Width of cavity
U_P	Amplitude of velocity of piston oscillations
V_S/V_N	Volume of exit slot/neck
C_S	Speed of sound in air
R_S	Surface resistance
Q	Volumetric flow rate of air at piston surface
Q_{OUT}	Volumetric flow rate of air through the exit slot
P_P	Pressure created on surface of piston
ϕ_A	Turns ratio of transformer used in electro-acoustic model to convert acoustic impedances to electric impedances
V	Voltage
I	Current
P_L	Useful power delivered to piston/load
P_E	Dissipation in motor armature windings
P_R	Power associated with rotor of motor
P_M	Power associated with rotation of crankshaft/belts/connecting rod
P_F	Friction in bearings of motor

P_{TOTAL}	Total power associated with motor/piston terms
Z_E	Electric impedance
Z_A	Acoustic impedance
V_{AC}	A/C voltage for electro-acoustic model
Ω	Frequency response function
T_M	D/C motor useful torque
K_T	Torque constant of motor
ω	Angular frequency of jet oscillations
R_M	Armature winding resistance of motor
Z_M	Impedance associated with D/C motor
I_R	Moment of inertia of rotor of motor about axis of rotation
I_M	Moment of inertia of crankshaft about axis of rotation
V_S	Motor supply voltage
I_S	Supply current of motor
Z_{EP}	Electric impedance of piston terms
Z_{EC}	Electric impedance of cavity terms
Z_{EN}	Electric impedance of neck/exit slot terms
M_{APair}	Acoustic mass of air moving with the piston
$M_{APpiston}$	Acoustic mass of piston and other moving parts of piston
M_{AP}	Total acoustic mass of piston terms
$R_{APpiston}$	Resistance associated with mechanical components of moving parts of piston
R_{APair}	Frictional resistance of the air moving with the piston
R_{AP}	Total acoustic resistance of piston terms
F_{MP}	Force experienced by piston and other moving parts of piston
V_C	Volume of cavity
C_{AC}	Acoustic compliance of air in the cavity
M_{AN}	Acoustic mass of air in the exit slot/neck
K_D	Jet dump loss coefficient
R_{AN}	Acoustic resistance of air in the exit slot/neck

- R_S Surface resistance of the air in the exit slot/neck
- R_{AL} Viscous losses associated with air in the exit slot/neck
- C_{AN} Acoustic compliance of air in the exit slot/neck

INTRODUCTION

This thesis presents a study of the compressibility effects on the performance of a D/C motor driven Synthetic Jet Actuator (SJA) for flow separation control. A theoretical model accounts for the compressibility and viscous/friction losses at the exit slot of the SJA. An electro-acoustic model to predict the frequency response of the SJA is also presented and this model should help formulate feedback optimal control strategies for real time flow control using an array of actuators.

A boundary layer is formed over the surface of a body moving in a viscous fluid and the particles in this layer are slowed by the friction between the fluid and the surface of the body. When an adverse pressure gradient is present in this flow field, both the wall shear forces and the pressure gradient will reduce the momentum of the fluid particles. This reduction in the momentum of the particles within the boundary layer will cause the flow to reverse its direction, downstream in the flow. Then, the viscous layer will depart from the surface, and the surface streamline closest to the surface will separate from the surface and the boundary layer is said to be separated.

The separation of the boundary layer is associated with large energy losses; therefore the separation point determines the performance of many devices. For example, if the separation of the boundary layer formed over a blunt body is delayed, the pressure drag is greatly reduced (Gillaranz and Rediniotis, 2001). An adequate method of delaying separation will permit the operation of a wing at higher angles of attack or a helicopter blade with a higher incidence angle. The delay or elimination of separation can be used to increase the pressure recovery in a diffuser (McCormick, D., 2000). Hence, separation control is of great importance to most systems involving fluid flow, such as air, land or sea vehicles, turbo machines, diffusers, etc.

Many researchers have developed and tested methods of separation control. Typically, separation control techniques may be of two types: passive and active. Several techniques developed for passive control of the boundary layer separation are discussed in Gad-el-Hak and Bushnell (1991).

This thesis follows the style and format of the *Journal of Fluid Mechanics*.

This research focuses on active flow control methodology.

A number of active separation control methods have been studied and developed. These include steady boundary layer suction to remove the low momentum fluid, wall heat transfer to control and modify the viscosity of the fluid, moving walls in order to use the no-slip condition at the surface to energize the fluid close to the wall, momentum addition to the boundary layer by steady blowing, and oscillatory blowing and suction methods.

The methods using oscillatory blowing and suction have proven to be more effective than just steady blowing or steady suction (Amitay et al., 1998). In recent years, the development of “synthetic jets” or “zero mass flux” devices has received a great amount of attention from the fluid dynamics research community. These systems involve small-scale, low-energy, typically high-frequency actuators, in which the operation is based on the concentrated input of energy at high receptivity regions of the flow field. They take advantage of the physical flow processes to amplify the applied disturbance, which stand apart from the traditional macro-scale control approaches.

The use of synthetic jet actuators for flow control and separation delay has been extensively examined by many researchers. Current research includes investigation of the performance of this technology to modify the lift, drag, and flight control characteristics of unconventional airfoils as well as flow separation over bluff bodies (Amitay et al., 1998; Smith et al., 1998; Seifert et al., 1993; Seifert et al., 1996; Seifert and Pack, 1999). Most of the previously developed synthetic jet actuators (SJA) are either piezoelectricity driven or are powered from external hardware making them very bulky and requiring a lot of tubing and plumbing to generate the required power for operation (Seifert et al., 1998; Rathnasingham and Breuer, 1997). For example, in both Greenblatt and Wagnaski (1998) and Seifert and Pack (1999), the mechanism used to generate the pressure oscillations necessary for the zero-mass-flux flow control was a hardware-intensive mechanism, with most of the hardware residing outside the test section. These pressure oscillations were generated outside the test section and the model, and were directed into the model through plumbing. For most air or water

applications, the SJAs need to be compact in order to be housed inside the control surface of the body where the aerodynamic/hydrodynamic characteristics are being modified. The piezoelectric actuators, though compact, do not perform efficiently at frequencies away from the actuator resonance frequencies, have limited maximum amplitudes, and their performance generally deteriorates at off-design conditions (Gillaranz and Rediniotis, 2001). The D/C motor driven actuator is very compact and can be seated easily inside a wing and can operate at frequencies as high as 150 Hz producing high jet velocities. These motor driven actuators have been used to control or completely eliminate separation over an airfoil even in the post-stall regime (Gillaranz and Rediniotis, 2001).

For these actuators, the driving motor has to supply enough power to overcome both the fluid pressure forces and the inertial forces of the moving parts of the actuator. Moreover, the size of the actuator needs to be miniaturized to be embedded inside the control surface. This miniaturization requires knowledge of the physical mechanisms through which the actuator influences flow separation. Modeling these physical mechanisms individually will help optimize the performance of the actuator. The influence of the geometric parameters on the performance of the actuator also helps optimize the actuator design.

The basic principle behind a synthetic jet actuator is that the motor drives a piston into oscillation, which produces a zero-mass-flux jet within the cavity. The oscillatory jet adds momentum to the boundary layer in two ways: During the suction part of the cycle, it draws the low momentum fluid in the boundary layer inside the cavity, thereby bringing the higher momentum fluid, at the boundary layer edge, near the control surface. On the other hand, during the blowing part of the cycle, it adds the same fluid with higher momentum to the flow, almost tangentially to the control surface. The average effective momentum added over the entire cycle replenishes the momentum deficit in the boundary layer. Therefore the actuator, not only produces momentum itself, but also enhances the ability of the boundary layer to overcome adverse pressure gradients downstream through the mixing it induces of the low momentum fluid near the

surface with the high momentum external flow. The effectiveness of this mixing process is expected to relate to the high receptivity of the shear layer emanating from the point of separation. Proper excitation of the shear layer promotes the development of its natural instability, which forms large vortical coherent structures (Gillaranz and Rediniotis, 2001). These flow structures promote boundary layer mixing and hence momentum exchange between the outer and inner parts of the boundary layer.

Most previous researchers have assumed the flow of the jet within the actuator to be incompressible. The current model of the actuator can operate at frequencies as high as 150 Hz exhibiting deviation from the performance predicted by the assumption of incompressibility. The current study of the compressibility effects of the actuator flow characterizes the effects of the actuator parameters, such as actuator geometry, motor driving frequency, and oscillation amplitude on the flow. The objective of this research is to maximize flow reattachment at reasonable oscillatory blowing momentum coefficients. Most previous researchers have used a circular orifice to enable momentum mixing. The current SJA model tested and analyzed in this thesis uses a rectangular orifice and the edge of the cavity where the flow changes direction towards the exit slot plane is smoothed to minimize flow separation. Different slot widths, cavity volumes, and piston parameters are tested to quantify the effects of geometry on the performance of the actuator. The theoretical model accounting for the compressibility effects is then validated with hot wire anemometer experiments conducted under similar conditions.

A comprehensive method to predict the effects of the actuator parameters, such as actuator geometry, location, frequency, amplitude, on the flow needs to be developed. The electro-acoustic model presented here should help formulate feedback optimal control strategy for real time flow control using an array of actuators. The SJA physical mechanism involves so many parameters that it has always been complex to develop a mechanical model to predict the performance of the actuator. Electrical elements are easier to model compared to mechanical elements and the electro-acoustic model developed here should help quantify the effects of actuator parameters on the fluid flow. This will help develop an appropriate design of the actuator to achieve maximum flow

separation control. In addition, feedback control applications require the frequency response function that relates the input voltage to the output quantity of interest in the control system. This output quantity in our case is the volumetric flow rate of air through the exit slot. The analysis and design of coupled-domain transducer systems are commonly performed using lumped element models (Fischer, 1955; Hunt, 1982; Rossi, 1988). McCormick (2000) employed Lumped Element Modeling to speaker-driven synthetic jets, whereas Rathnasingham and Breuer (1997) were the first to develop a low-order model of a synthetic jet actuator. Louis Cattafesta et al. (2002) have applied LEM to Piezoelectric-driven synthetic jet actuators. To the author's knowledge, this research work represents the first application of electro-acoustic modeling to D/C motor-driven SJAs.

In the theory of electric oscillation there are three basic circuit elements. Capacitance stores electrical energy, inductance stores magnetic energy and ohmic resistance dissipates energy. The energy per unit time that is received by a storage element or transformed into heat by a resistive element is the instantaneous electric power. This power is the product of the terminal voltage and the input current. In case of mechanical oscillation there are also two storage elements and one dissipative element. These are the mass, which stores kinetic energy, the compliance of a spring, which stores potential energy and the frictional resistance. Here, the instantaneous power is the product of two quantities, namely the force and the velocity. The comparison of the basic electrical equations and the basic mechanical equations suggests that there is a coupling between the electric and mechanical energy domains. The analogy yields the following conclusions: The force in a mechanic oscillator is equivalent to a voltage in an electric oscillator, the velocity is equivalent to the current, the mass is equivalent to the inductance, the compliance is equivalent to the capacitance, and the frictional resistance is equivalent to the ohmic resistance (Fischer, 1955). Based on these preliminary basic fundamentals of electro-mechanical coupling, the electro-acoustic model of the D/C motor-driven SJA will be developed. The term acoustic has been used here because the motor driving voltage creates an effective acoustic pressure, which drives the piston into

motion, causing the jet to be produced. Hence the driving voltage of the electro-acoustic circuit should be large enough to overcome the acoustic pressure to create the oscillatory jet. Elements that have a common effort or energy or force, as in our case, are connected in parallel and elements that share a common velocity or current or flow rate, as in our case, are connected in series.

Each of the individual impedances is then analyzed and evaluated by equating the energies in the respective electrical and mechanical domains. The resulting equivalent circuit is then analyzed to understand the effects of geometry and material properties on important design parameters, such as resonance frequency and volume displacement per applied voltage. This model has some assumptions that are discussed in this work, which cause certain limitations. These limitations are discussed along with the results of experimental study that were designed to quantify the validity of this model.

Thus the primary objectives of this thesis are to provide a comprehensive study of the effects of compressibility on the performance of a D/C motor-driven synthetic jet actuator and also to develop a dynamic model to predict the frequency response function of the SJA and validate this model with experiments and also present a study of the effects of actuator parameters on its performance using this model.

EXPERIMENTAL FACILITIES

The experiments presented in this thesis were conducted in the Fluid Dynamics Laboratories of the Aerospace Engineering Department. Description of these facilities and the hardware and software instrumentation used is given below.

HOT WIRE ANEMOMETRY

The flow field velocity measurements were done using a constant-temperature hot wire anemometer. The anemometer measures fluid speed using a delicate probe made from a thin tungsten/platinum wire which is heated to a temperature higher than the average temperature of the fluid. Using electronic circuitry, the anemometer stabilizes and maintains the probe temperature at a constant level throughout the measurement. Because the anemometer must maintain the probe at a constant temperature, it is sensitive to the rate at which it is being cooled, i.e., the fluid velocity. This velocity is then translated into a continuously changing voltage, which has a non-linear relationship with the fluid velocity. This voltage signal then undergoes signal conditioning to filter out noise and improve the signal/noise ratio.

After proper calibration of the probe channels, it is possible to measure fluid velocities with an accuracy of 0.005% or greater, depending upon the measurement range and the quality of calibration. The response time between measurement and instrument output is very short in comparison with other methods of fluid flow measurement and can reach a minimum of 1.2 microseconds. This system can measure fluid velocities ranging from 0 to 150 m/s as well as supersonic measurements. In principle, the probe is connected to a Wheatstone bridge, which is almost balanced at room temperature. During operation, the feedback circuit is continuously trying to balance the bridge, causing a heating current to flow through and heat the probe, increasing its resistance to the point where the bridge is balanced again. The output voltage of the servo amplifier, which indicates the degree to which the probe is being heated, gives us a measure of the rate of cooling of the probe by the fluid, which is proportional to the fluid flow rate.

The hot wire had to be calibrated separately each time the experiment was performed. This calibration depends on the ambient temperature and hence this frequent calibration is necessary. The hot wires were calibrated using a TSI-1125 probe calibrator. This calibrator is designed primarily for air, and uses an air supply at 100 psi. It has three chambers and nozzles, and they can be used to calibrate the hot wires for velocities ranging from approximately 0.01 to 300 m/s. The accuracy of calibration is 0.005%. The velocity was measured at the center of the exit slot of the SJA. Because of the very small width of the slot, it was not possible to identify the center of the slot precisely. Hence, the exit velocity was measured at four different points along the slot width and the maximum of these velocities is taken as the velocity at the center of the slot. The frequency of the motor is varied from 0 to around 150 Hz and exit velocities as high as 120 m/s are measured using this hot wire anemometry system. An overheat ratio of 1.4 is used for the hot wire anemometer experiments.

SOFTWARE

Table 1 lists the software used in this research.

Program	Applications and Developer
Matlab V 5.3.0.10183(R11)	Technical Computing, Math Works Inc.
Maple V 6.00a	Technical Computing, Waterloo Maple Inc.
MathCAD Professional	Math Soft Inc.
Microsoft Office	Microsoft Corporation
AutoCAD Release 14	AutoCAD Corporation

TABLE 1. Software used in thesis.

STUDY OF COMPRESSIBILITY EFFECTS OF DC MOTOR DRIVEN SJAs

INTRODUCTION

Most previous researchers, in studying the performance of a synthetic jet actuator, have assumed the flow to be incompressible at the orifice. As the size of the exit slot becomes smaller, the compressibility effects become predominant and the SJAs do not perform as efficiently and provide very low jet velocities not suitable to achieve efficient flow reattachment. Also, the SJA currently being tested is the first DC motor-driven actuator to be developed according to the author's knowledge and as stated previously, it has many advantages over piezoelectric actuators. One advantage is that the amplitude of jet oscillation can be of the order of millimeters and also the current SJA is compact with very little piping/plumbing and can be easily seated inside a wing. Also, the actuator performs efficiently even at frequencies away from the resonance frequency. Very high exit velocities at low frequencies can be achieved with this new DC-motor driven SJA and also the SJA can be operated at variable frequencies permitting tuning of the actuator frequency to the frequency at which actuation is optimal.

The two main parameters that need to be considered while designing an actuator for flow separation control are the blowing momentum coefficient $\langle C_{\mu} \rangle$ and the design forcing frequency (F^+). The optimum design frequency for maximum flow separation control is around 1 and our objective is to achieve maximum flow reattachment at reasonable blowing momentum coefficient values (Gillaranz and Rediniotis, 2001).

The non-dimensional frequency, F^+ , is a measure of the number of cycles of actuation during the time the freestream travels one chord length, and is defined in terms of the actuator frequency as

$$F^+ = \frac{f \cdot C}{U_{\infty}} \quad (1)$$

The oscillatory blowing momentum coefficient, C_μ is defined as the ratio of the root mean square value (RMS) of momentum addition from the oscillating jet to the momentum in the freestream, and is expressed as

$$C_\mu = \frac{(\rho \cdot S_W \cdot U_\infty^2)_{JET}}{(\rho \cdot h \cdot U_\infty^2)_\infty} \quad (2)$$

In the above equation, h is some characteristic length (maybe the chord length of the airfoil).

These two non-dimensional parameters measure the performance of the SJA and can be used as tools to design the actuator mechanism. The optimal design involves computation of chamber geometry and slot geometry and the operating conditions such as frequency and amplitude of oscillation. Different cavity volumes and different slot geometries have been tested in this research to optimize the design and performance of the SJA. Major emphasis in this analysis has been given to the effects of frequency of oscillation, exit slot width and cavity volumes on the SJA performance. Based on this analysis, the design of the SJA needs to be improved to maximize performance.

THEORETICAL MODEL TO PREDICT COMPRESSIBILITY EFFECTS

MODEL WITHOUT ACCOUNTING FOR FRICTION LOSSES AT EXIT

Most previous researchers, as stated earlier, have assumed the flow in the exit slot of an SJA to be incompressible. However, it is important to study the compressibility effects of the flow in the exit slot to understand the dynamics of the SJA operation completely.

Figure 1 shows a schematic of a typical synthetic jet actuator.

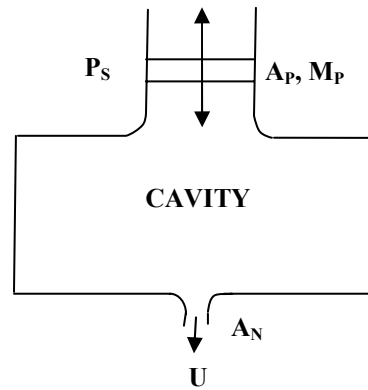


FIGURE 1. General schematic of a synthetic jet actuator.

The following analysis presents a theoretical model to predict the compressibility effects of the jet at the exit.

The displacement and velocity of the piston oscillations at any instant of time are expressed as

$$x = A.[1 - \cos(2.\pi.f.t)] \quad (3)$$

$$\dot{x} = 2.A.\pi.f.\sin(2.\pi.f.t) \quad (4)$$

A is the amplitude of the piston oscillation, which is one half the stroke of the piston.

$$\text{Volume of air inside the cavity} = V_O - A_P \cdot x$$

We consider both the suction and blowing cycle for this analysis. During the suction part of the cycle, mass is added to the system and during the blowing part of the cycle, mass is removed from the system.

Hence, the mass flow rate through the system is positive during the suction cycle and negative during the blowing cycle.

$$\frac{dm}{dt} = -\rho \cdot A_S \cdot U \quad (5)$$

$$\text{Mass of air in the system} = \rho \cdot (V_O - A_P \cdot x)$$

Differentiating this and equating it to the mass flow rate,

$$-\rho \cdot A_S \cdot U = \frac{d}{dt} [\rho \cdot (V_O - A_P \cdot x)] \quad (6)$$

$$-\rho \cdot A_S \cdot U = -\rho \cdot A_P \cdot \dot{x} + \dot{\rho} \cdot (V_O - A_P \cdot x) \quad (7)$$

Rearranging this,

$$\frac{\dot{\rho}}{\rho} = \frac{A_P \cdot \dot{x}}{(V_O - A_P \cdot x)} - \frac{A_S}{(V_O - A_P \cdot x)} \cdot U \quad (8)$$

We introduce the constants $c1$ and $c2$ as

$$c1 = \frac{A_P \cdot \dot{x}}{(V_O - A_P \cdot x)} \quad (9)$$

$$c2 = \frac{A_S}{(V_O - A_P \cdot x)} \quad (10)$$

Hence,

$$\frac{\dot{\rho}}{\rho} = c1 - c2 \cdot U \quad (11)$$

When the flow is incompressible,

$$\dot{\rho} = 0$$

Hence the jet exit velocity equation for incompressible flow simplifies to

$$U = \frac{c_1}{c_2} = \frac{A_p}{A_s} \cdot \dot{x} \quad (12)$$

The above equation suggests that for incompressible flow, the jet exit velocity is a linear function of the motor frequency as expected. Appendix A gives the MathCAD code used to solve this equation for incompressible flow.

At higher frequencies of operation though, the flow is not incompressible and also smaller slot widths make the flow more compressible and hence a comprehensive study of the compressibility effects would help optimize the design to minimize the compressibility effects.

As derived earlier, for compressible flow

$$\frac{\dot{\rho}}{\rho} = c_1 - c_2 \cdot U \quad (13)$$

Now we assume that the air has zero velocity at the center of the cavity. The air inside the cavity has very low momentum.

Applying the unsteady Bernoulli's equation between the center of the cavity and the exit slot,

$$\nabla \left(\dot{\phi} + \frac{p}{\rho} + \frac{U^2}{2} \right) = 0 \quad (14)$$

which upon expansion between the center of the cavity and the exit slot yields,

$$p_c - p_o = \frac{1}{2} \cdot \rho \cdot U^2 + \rho \cdot (\dot{\phi}_o - \dot{\phi}_c) \quad (15)$$

The subscript "o" represents exit slot terms and the subscript "c" represents cavity terms. The exit slot is open to the atmosphere and hence it is at ambient pressure.

The velocity potential at the exit slot can be evaluated from the following expression.

$$\phi_o = \phi_c + \int \left(\frac{d\phi}{dx} \right) \cdot dx = \phi_c + U \cdot l \quad (16)$$

where l is the acceleration length of the exit slot.

We assume the acceleration length is a multiple of the slot width, hence,

$$\dot{\phi}_o - \dot{\phi}_c = \dot{U}l \quad (17)$$

Substituting equation (17) in equation (15), we get

$$p_c = p_o + \frac{1}{2} \cdot \rho \cdot U^2 + \rho \cdot \dot{U}l \quad (18)$$

During the blowing part of the cycle, $1/2\rho U^2$ is positive and during the suction part of the cycle it is negative.

Hence to account for both blowing and suction,

$$\frac{1}{2} \cdot \rho \cdot U^2 = \frac{1}{2} \cdot \rho \cdot U \cdot |U| \quad (19)$$

which gives

$$p_c = p_o + \frac{1}{2} \cdot \rho \cdot U \cdot |U| + \rho \cdot \dot{U}l \quad (20)$$

Assuming the air inside the cavity to be isothermal, we get

$$\begin{aligned} p_c &= \rho \cdot R \cdot T \\ \dot{p}_c &= \dot{\rho} \cdot R \cdot T \end{aligned} \quad (21)$$

Differentiating equation (20) and substituting for \dot{p}_c from (21) yields

$$\dot{\rho} \cdot R \cdot T = \frac{1}{2} \cdot \rho \cdot \frac{d}{dt}(U \cdot |U|) + \rho \cdot \ddot{U}l + \dot{\rho} \cdot \dot{U}l + \dot{\rho} \cdot \frac{U \cdot |U|}{2} \quad (22)$$

Dividing by ρ and substituting for $\frac{\dot{\rho}}{\rho}$ from (13), we get

$$c1 \cdot (R \cdot T - \frac{U \cdot |U|}{2} - \dot{U}l) - c2 \cdot (U \cdot R \cdot T - \frac{U^2 \cdot |U|}{2} + U \cdot \dot{U}l) - \ddot{U}l - \frac{1}{2} \cdot \frac{d}{dt}(U \cdot |U|) = 0 \quad (23)$$

Equation (23) represents the jet exit velocity equation for compressible flow without accounting for friction losses and separation effects at the exit slot. This equation is solved using finite difference method for different frequencies of the motor.

The boundary conditions used are,

At $t = 0$, jet exit velocity = 0 and velocity acceleration at exit = 0

The jet exit velocity is also a periodic function of time. We are interested only in the maximum velocity generated. Hence, the amplitude of the jet exit velocity is plotted as a function of the actuator frequency for both compressible and incompressible flow for different slot geometries and different cavity volumes. The effect of the acceleration length, l , on the flow is also studied.

RESULTS AND DISCUSSION

The jet exit velocity is plotted for different motor frequencies. Table 2 gives a list of the different slot geometries and the cavity volumes that were tested using this analysis.

Piston Diameter (inches)	Piston Stroke (inches)	Exit Slot Width (inches)	Exit Slot Length (inches)	Cavity Width (inches)
0.906	0.811	0.032	2.5	0.3
0.906	0.811	0.032	2.5	0.4
0.906	0.811	0.032	2.5	0.5
0.906	0.811	0.064	2.5	0.3
0.906	0.811	0.064	2.5	0.4
0.906	0.811	0.064	2.5	0.5

TABLE 2. Different geometric parameters of SJAs tested for compressibility effects.

Figures 2 and 3 represent the design of the exit slot and the cavity of the SJAs that were analyzed.

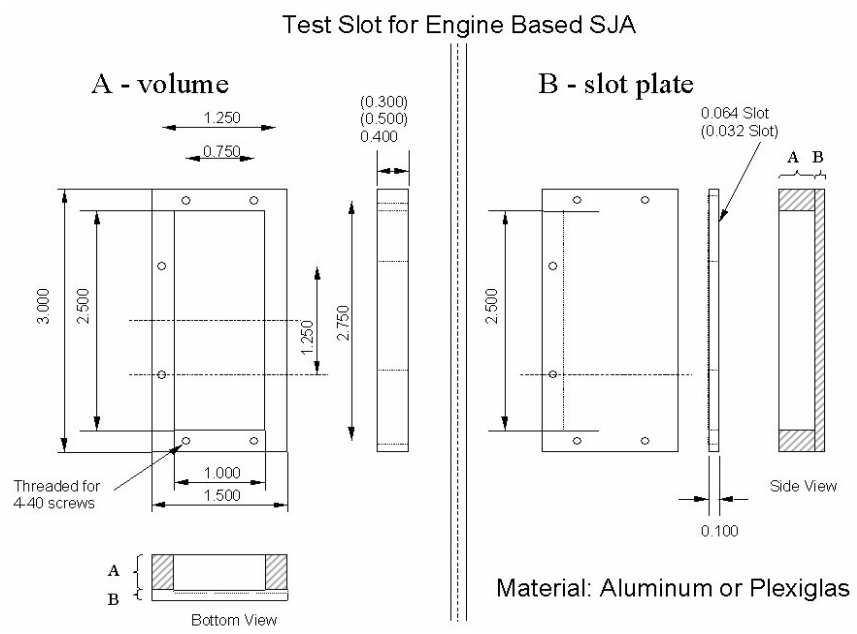


FIGURE 2. Design of SJA exit slot / cavity.

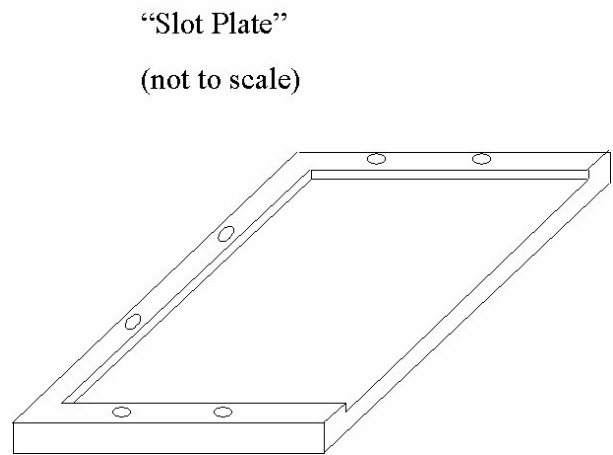


FIGURE 3. Design of exit slot plate.

Figure 4 represents the comparison between the theoretical compressible and incompressible jet exit velocity for both slot widths.

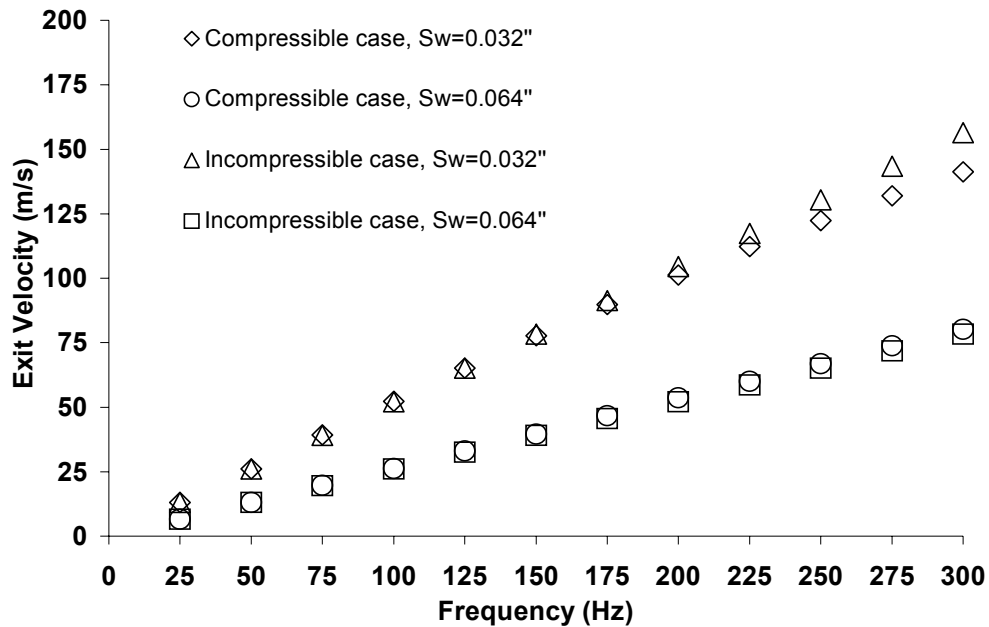


FIGURE 4. Jet exit velocity comparison for incompressible and compressible flow.

Figure 4 shows that as expected, the compressible case velocity is lesser than the incompressible case for both slot widths and also the smaller slot width has a higher velocity (both incompressible and compressible case) than the larger slot width, which is also expected.

Also this plot shows that compressibility effects are more predominant at larger frequencies and the flow tends to be more incompressible at smaller frequencies. Hence, the study of compressibility effects on the performance of the SJA is very important at

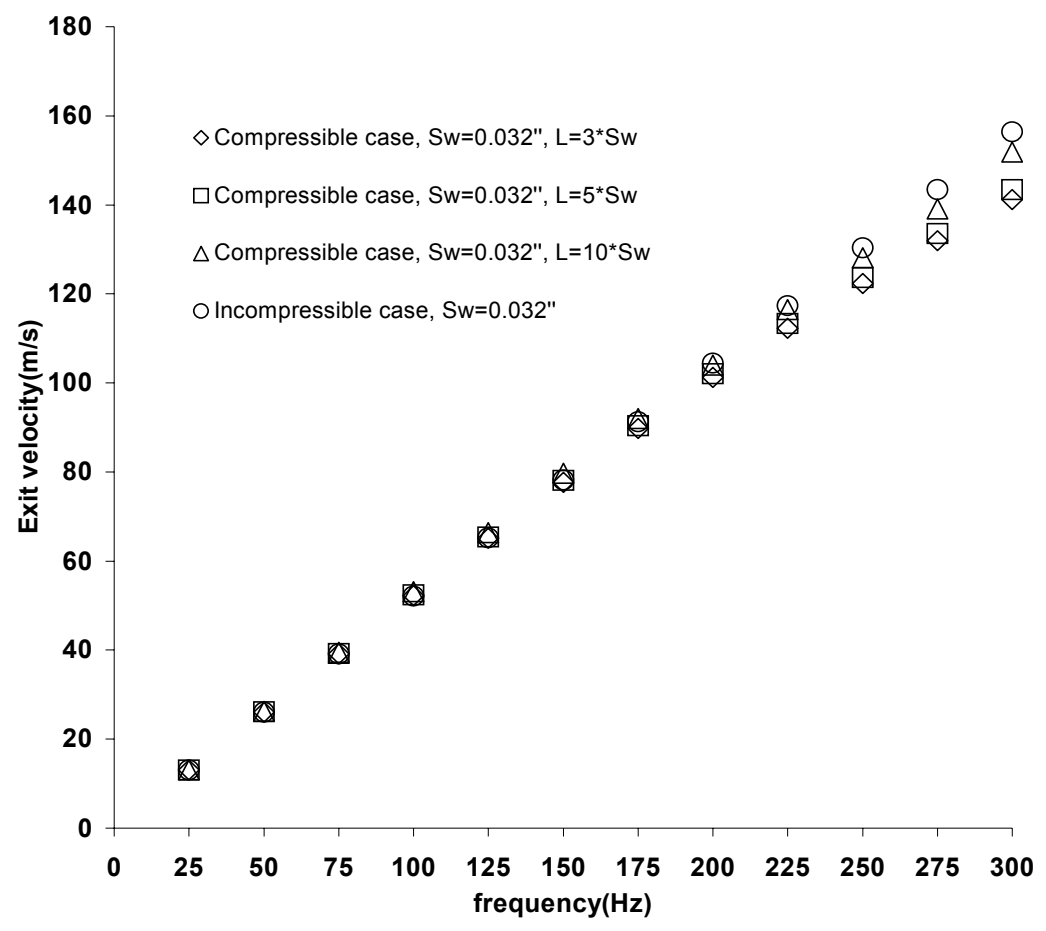


FIGURE 5. Exit velocity comparison between compressible and incompressible flow for different acceleration lengths.

higher frequencies and helps formulate an appropriate model to optimize the design of the SJA.

Figure 5 shows the variation of exit velocity with acceleration length for both theoretical compressible and incompressible flow for a slot width of 0.032 inches.

Figure 5 shows that the acceleration length does not have much of an effect on the jet exit velocity at lower frequencies, and at higher frequencies the jet exit velocity increases with increase in acceleration length. Based on the previous plot, the compressibility effects are more dominant at higher frequencies thus reducing the jet exit velocity and hence the lower acceleration length of $3*S_w$ is assumed hereafter for this model.

Figures 6 and 7 represent variation of the exit velocity with cavity volume for both slot widths.

Based on Figures 6 and 7, we can conclude that the cavity volumes tested do not change the jet exit velocity too much. More drastic cavity volume changes are necessary to see a more prominent change in the velocity. It is however observed that the jet exit velocity decreases marginally with the increase in cavity volume at higher frequencies for both slots.

Figure 8 represents the maximum and minimum pressure distribution at the center of the cavity.

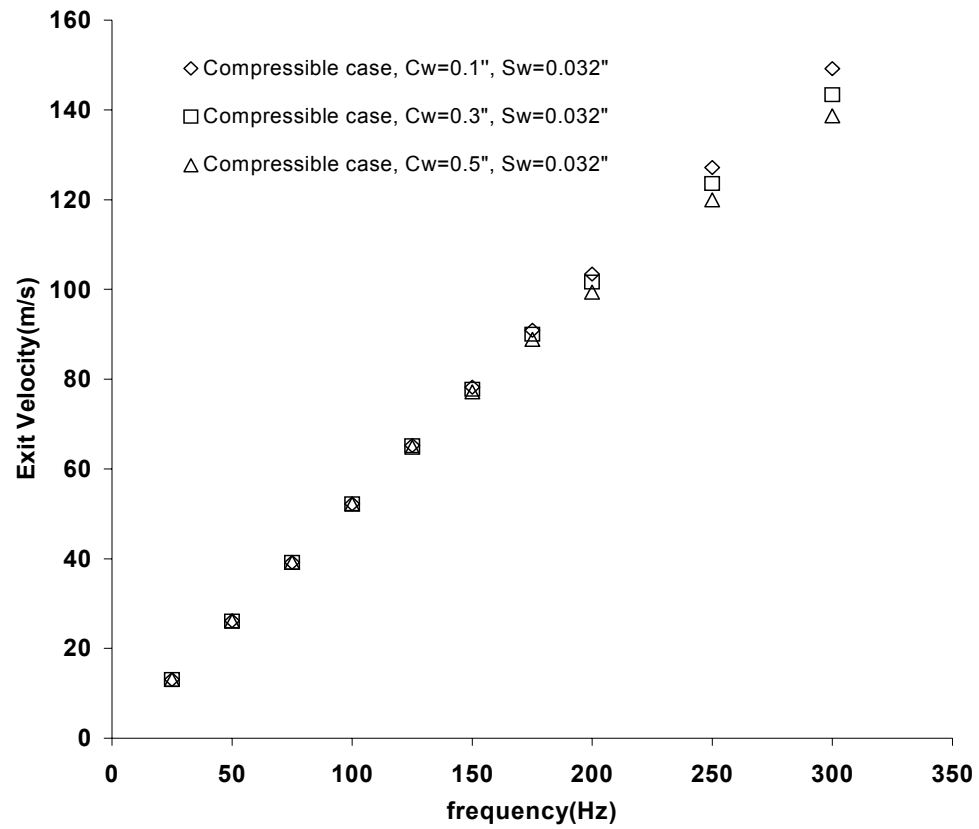


FIGURE 6. Variation of jet exit velocity with cavity volume for slot width 0.032".

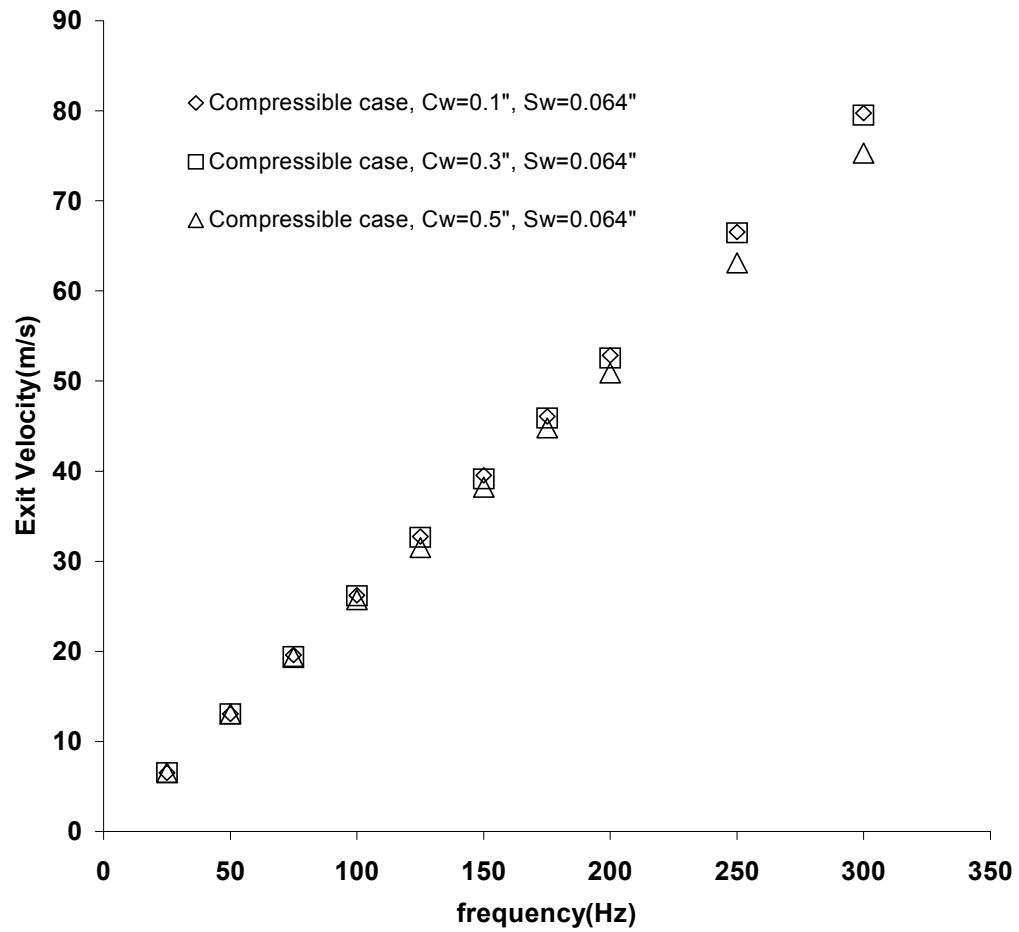


FIGURE 7. Variation of jet exit velocity with cavity volume for slot width 0.064".

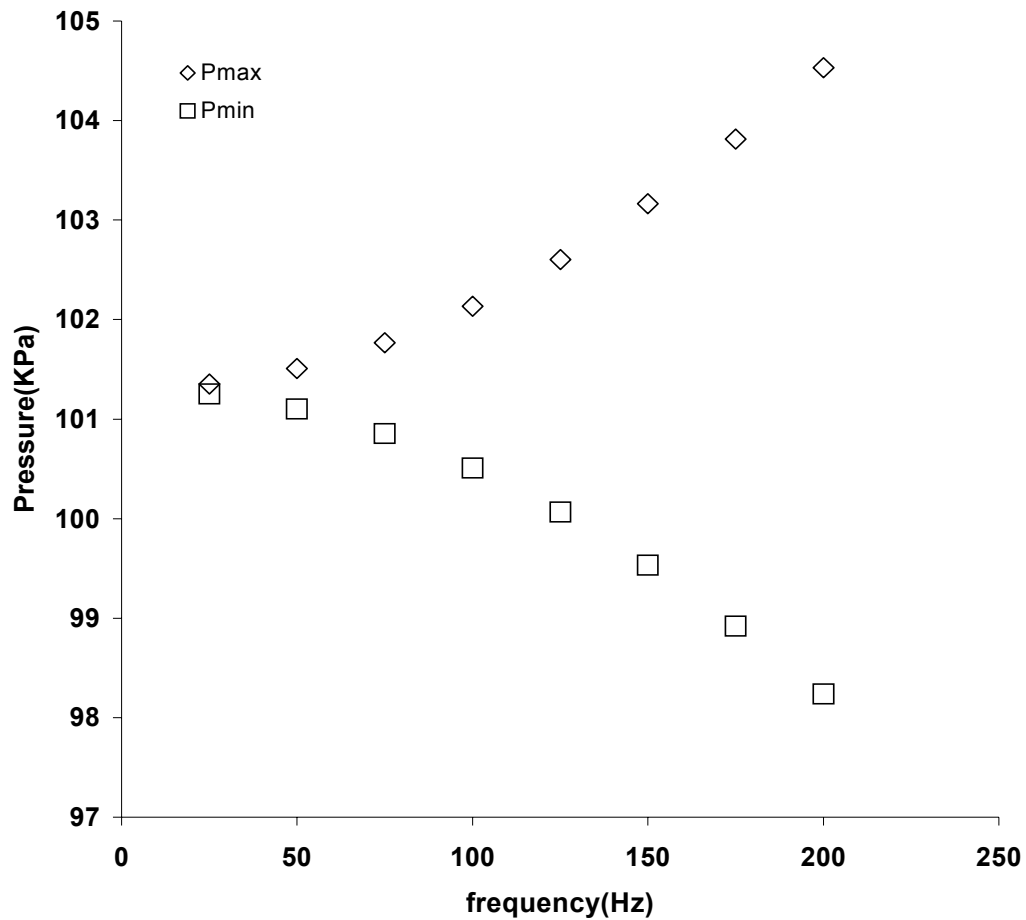


FIGURE 8. Variation of maximum and minimum pressure at the center of the cavity.

This model is also used to analyze the performance of a new six-cylinder SJA being currently developed and tested in the wind tunnel. The volume of the cavity is reduced due to the curvature on the corners of each of the six cavities in this case. This reduction is calculated and subtracted from the total cavity volume using integration with the geometry of the curvature being known. Two DC motors are used to run this six-cylinder SJA.

Table 3 lists the parameters of this new six-cylinder SJA that was tested using this model.

Piston Diameter (Inches)	Piston Stroke (Inches)	Slot Length (Inches)	Slot Width (Inches)
1.091	0.866	1.61	0.075

TABLE 3. Geometric parameters of six-cylinders SJA tested with model.

Figure 9 compares the compressible jet exit velocity and the incompressible case.

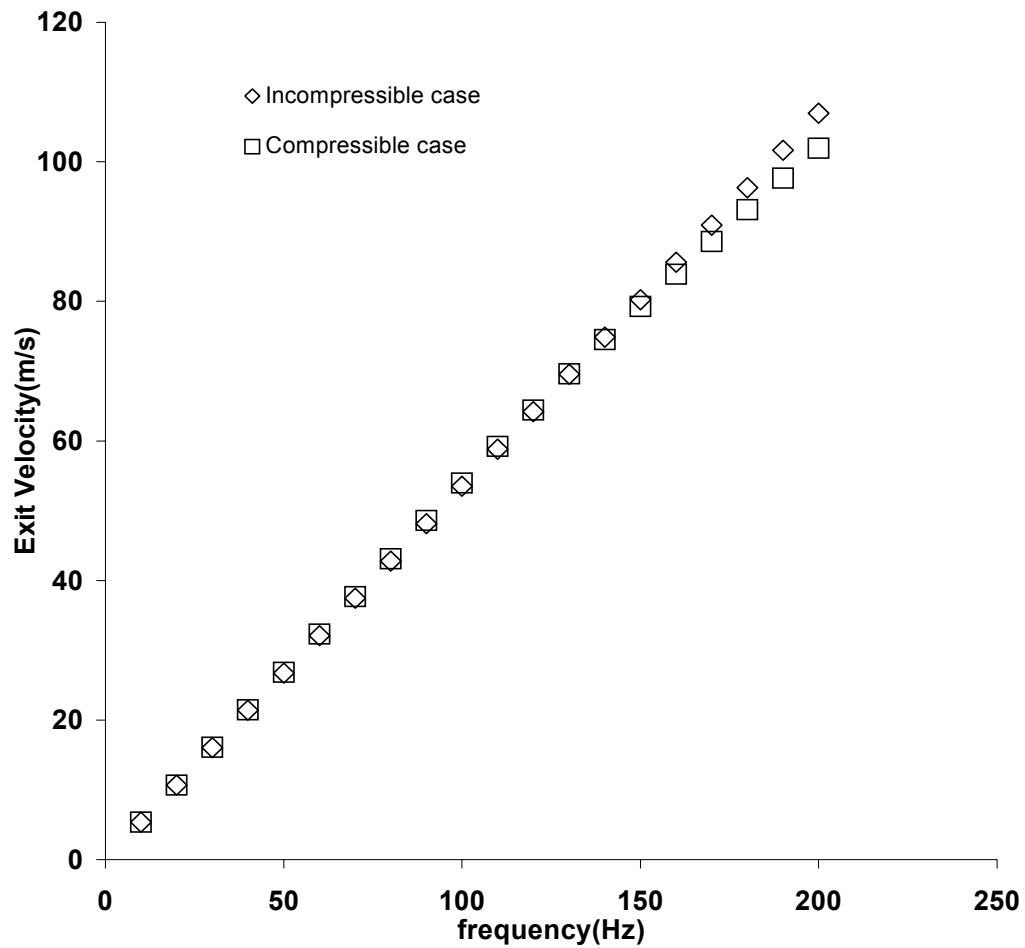


FIGURE 9. Jet exit velocity comparison between compressible and incompressible case for six-cylinders SJA.

As observed earlier, the compressible velocity is less than the incompressible velocity and also the compressibility effects are more predominant at higher frequencies.

Figure 10 represents the variation of exit velocity for compressible case with the cavity volume for the six cylinders SJA. The cavity volume is increased 10, 20 and 30% of its original value to generate these plots.

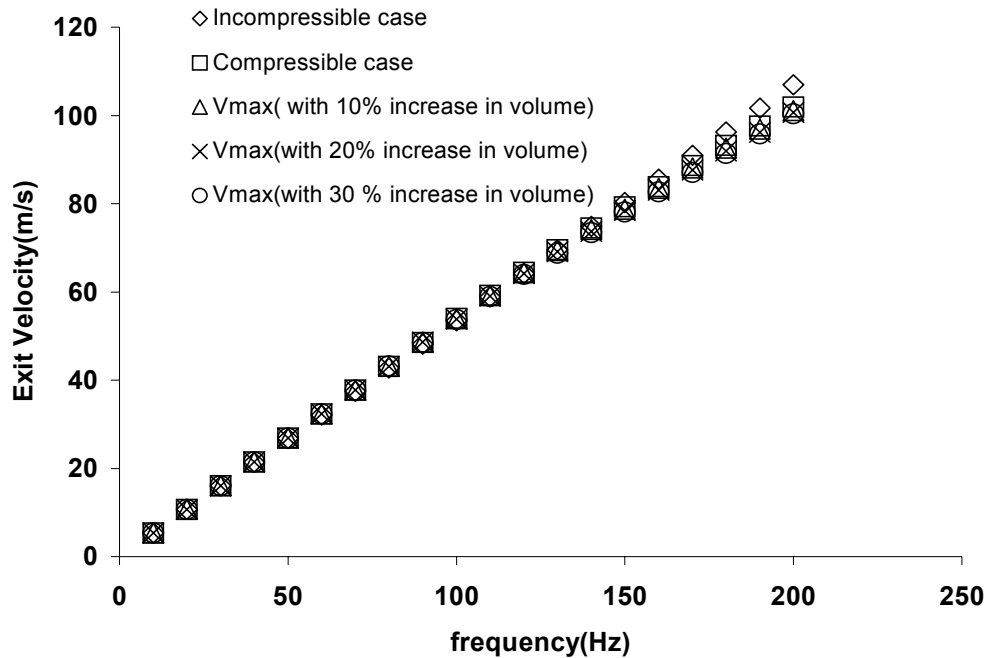


FIGURE 10. Variation of exit velocity with 10, 20 and 30 % increase in cavity volume for six-cylinders SJA.

Figure 10 shows that a higher cavity volume shows more compressibility effects compared to a smaller volume. The same phenomenon was also observed in the cavity volumes tested with the single-cylinder SJA and this new model with increased cavity volumes seems to produce the same behavior of the jet exit velocity variation thus reiterating the conclusion that reducing the cavity volume would decrease compressibility effects and produce a larger velocity of the jet.

Also, it can be seen that at smaller frequencies, the cavity volume does not have too much of an effect on the jet velocity as observed with the single-cylinder SJA.

Figure 11 represents the variation of jet exit velocity with cavity volume with the cavity volume decreased 10, 20 and 30% of its original value.

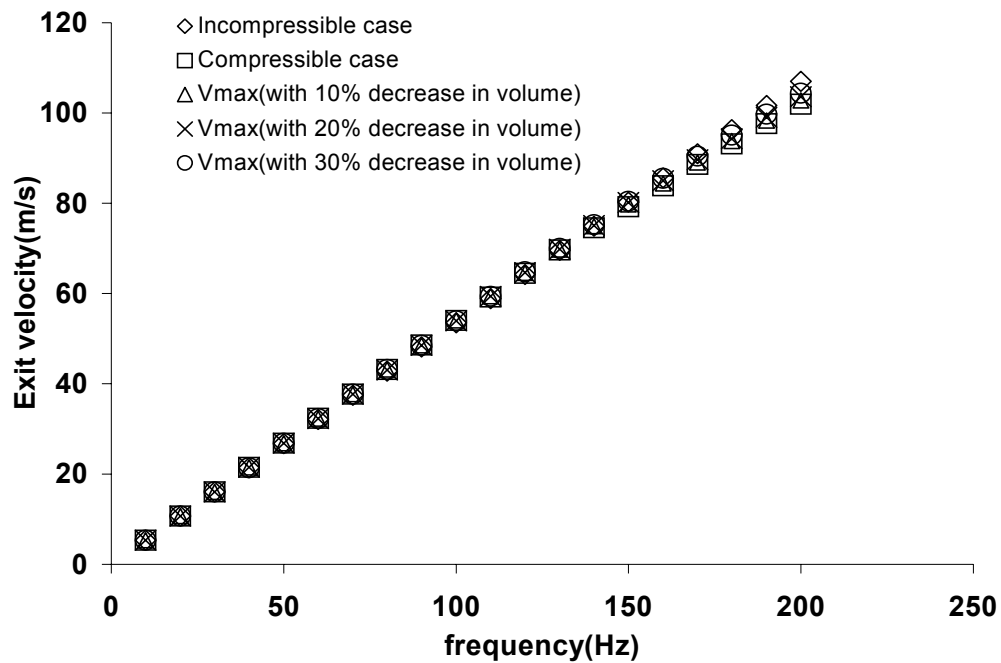


FIGURE 11. Variation of jet exit velocity with 10, 20 and 30 % decrease in cavity volume for six-cylinders SJA.

The same trend as the previous case with the increase in cavity volume is observed here, with the higher cavity volume tending to be more compressible than the lower cavity volume. It should however be noted that with 30% decrease in volume, the jet exit velocity approaches incompressible flow. The optimal design of the cavity would hence suggest that a smaller cavity volume would result in larger jet exit velocities.

Figure 12 represents the maximum and minimum pressure at the center of the cavity for this six-cylinder SJA case.

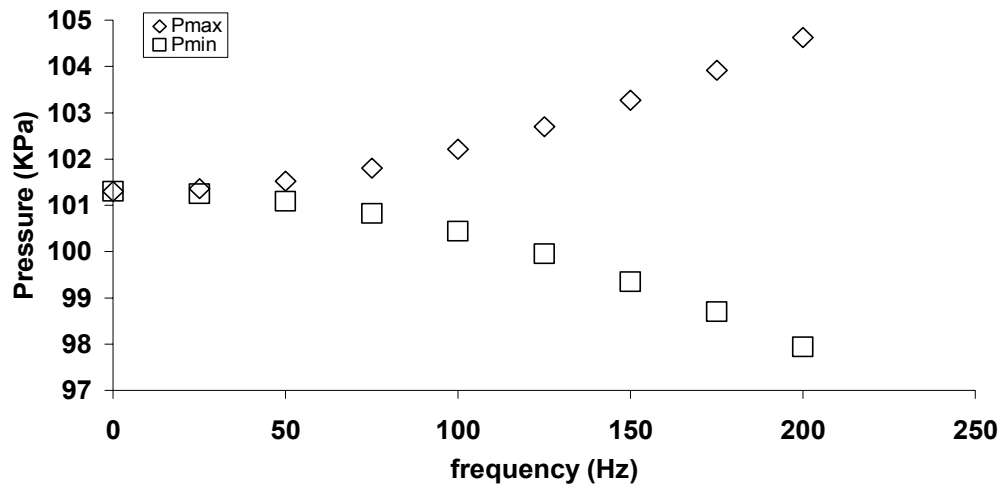


FIGURE 12. Maximum and minimum pressure at center of cavity.

It should be noted here, however, that this model does not account for any viscous losses that occur at the exit slot and also any separation effects that might reduce the velocity. The next section discusses the model accounting for both the viscous losses and the separation effects.

MODEL ACCOUNTING FOR FRICTION LOSSES AND SEPARATION EFFECTS AT EXIT

This section presents a theoretical model to predict the jet exit velocity with viscous losses and flow separation effects at the exit slot plane taken into account.

Friction losses in the throat and flow separation at the exit plane of the slot cause damping. The line integral of the momentum equation along a streamline relates the exit velocity to the pressure inside the cavity (Michael et al. 2000). Boundary layer separation occurs at the exit slot plane where the flow curves around the cavity edge to enter the slot. The line integral is evaluated between the cavity and the exit plane of the slot and the resulting equation is (Michael et al. 2000)

$$\rho \cdot \frac{d}{dt} \left(\int U \cdot ds \right) + \rho \cdot \int \left[\nabla \left(\frac{U^2}{2} + p \right) \cdot ds \right] = -\mu \cdot \int (\nabla \times \omega) ds \quad (24)$$

After integrating this equation, during the blowing part of the cycle, we get

$$\frac{dU}{dt} = \frac{p}{L_e \cdot \rho} - \frac{U^2}{2 \cdot C_d^2 \cdot L_e} - \frac{8 \cdot \mu \cdot U \cdot L_v}{\rho \cdot L_e \cdot h_t^2} \quad (25)$$

During the suction part of the cycle,

$$\frac{dU}{dt} = \frac{p}{L_e \cdot \rho} + \frac{U^2}{2 \cdot C_d^2 \cdot L_e} - \frac{8 \cdot \mu \cdot U \cdot L_v}{\rho \cdot L_e \cdot h_t^2} \quad (26)$$

In the above equations, L_e represents the equivalent inertia length of the exit slot, L_v represents the equivalent viscous length of the slot, h_t represents the height or the width of the slot and C_d is the flow coefficient associated with the streamline curvature at exit.

To account for both suction and blowing in the same equation, we can write the equation for the exit velocity as

$$\frac{dU}{dt} = \frac{p}{L_e \cdot \rho} - \frac{U \cdot |U|}{2 \cdot C_d^2 \cdot L_e} - \frac{8 \cdot \mu \cdot U \cdot L_v}{\rho \cdot L_e \cdot h_t^2} \quad (27)$$

Here p represents the relative pressure in the cavity = $p_c - p_o$

Differentiating equation (27) with respect to time,

$$\ddot{U} = \frac{p_o \cdot \dot{p}}{L_e \cdot \rho^2} - \frac{d}{dt} (U \cdot |U|) - \frac{8 \cdot \mu \cdot L_v \cdot \dot{U}}{\rho \cdot L_e \cdot h_t^2} + \frac{8 \cdot \mu \cdot L_v \cdot U \cdot \dot{p}}{\rho^2 \cdot h_t^2 \cdot L_e} \quad (28)$$

We substitute $p_o = \rho \cdot R \cdot T_o$ and for $\frac{\dot{p}}{\rho}$ from (13) and introduce the constant c as

$$c = \frac{8 \cdot \mu \cdot L_v}{L_e \cdot h_t^2} \quad (29)$$

Rearranging equation (28) after the above mentioned substitutions yields,

$$\ddot{U} = \frac{c1 \cdot R \cdot T_o}{L_e} - \frac{c2 \cdot R \cdot T_o \cdot U}{L_e} - \frac{d}{dt} (U \cdot |U|) - \frac{c \cdot R \cdot T_o \cdot \dot{U}}{p_o} + \frac{c1 \cdot c \cdot U \cdot R \cdot T_o}{p_o} - \frac{c \cdot c2 \cdot R \cdot T_o}{p_o} \quad (30)$$

The above equation is solved for the jet exit velocity using finite difference

method and the velocity is plotted as a function of frequency. This exit velocity is compared with the case where the friction losses are neglected and boundary layer separation has also been ignored.

Appendix B gives the MathCAD code used to solve this equation using finite difference method.

DETERMINING THE CONSTANT, c

Let us now try to evaluate the constant, c , which is dependent on the geometry of the SJA and the flow properties.

$$c = \frac{8 \cdot \mu \cdot L_v}{L_e \cdot h_t^2} \quad (31)$$

L_e = equivalent inertia length = $L_t + (A_s \cdot \pi / 4)^{1/2}$

h_t = Resonator throat height = width of the exit slot

L_v = equivalent viscous length of the throat = Acceleration length of air in the exit

As of now, the only information we have is $L_v \leq L_t$, Hence we assume $L_v = k \cdot L_t$, where $L_t = S_L$

The variation of C_d with frequency and the geometry/ dimensions of the exit slot was studied and the results of this study and its effects on this new model accounting for friction losses at the exit are presented in the following section.

RESULTS AND DISCUSSION

The behavior of the jet exit velocity with the friction losses at the exit taken into account is studied and it is observed that C_d might be a function of the frequency of oscillation. The variation of C_d is studied and its effects on the exit velocity are observed.

Figure 13 represents the variation of jet exit velocity between the incompressible case, the theoretical compressible model without accounting for friction losses at the exit and the model accounting for friction/viscous losses, for a slot width 0.032" inches.

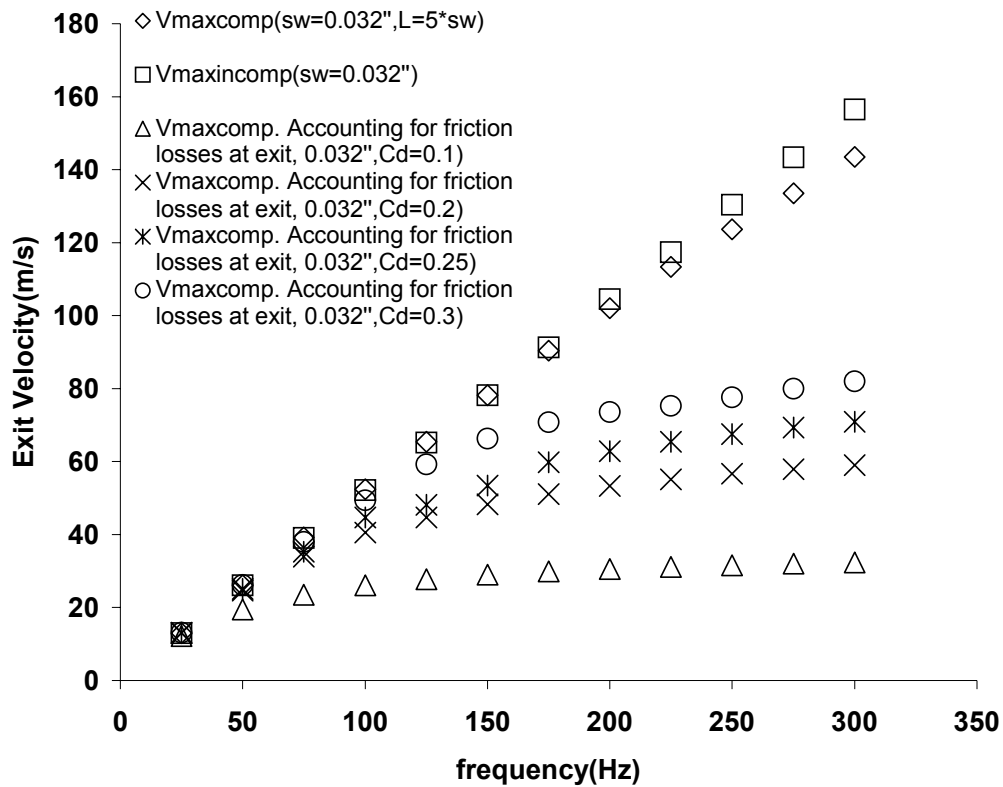


FIGURE 13. Jet exit velocity comparison between incompressible and compressible cases with and without friction losses for slot width 0.032".

From the above plot, we can see that at lower frequencies, the effects of friction/viscous effects are smaller. At higher frequencies however, the viscous effects predominate and need to be considered while modeling the SJA. Also, the variation of jet exit velocity with C_d was presented above and the jet exit velocity decreased drastically with decrease in C_d at higher frequencies suggesting that lower values of C_d represent very high viscous losses and flow separation effects at the exit.

Figure 14 represents the variation of jet exit velocity between the incompressible case, the theoretical compressible model without accounting for friction losses and the model accounting for friction/viscous losses, a slot width 0.064” inches.

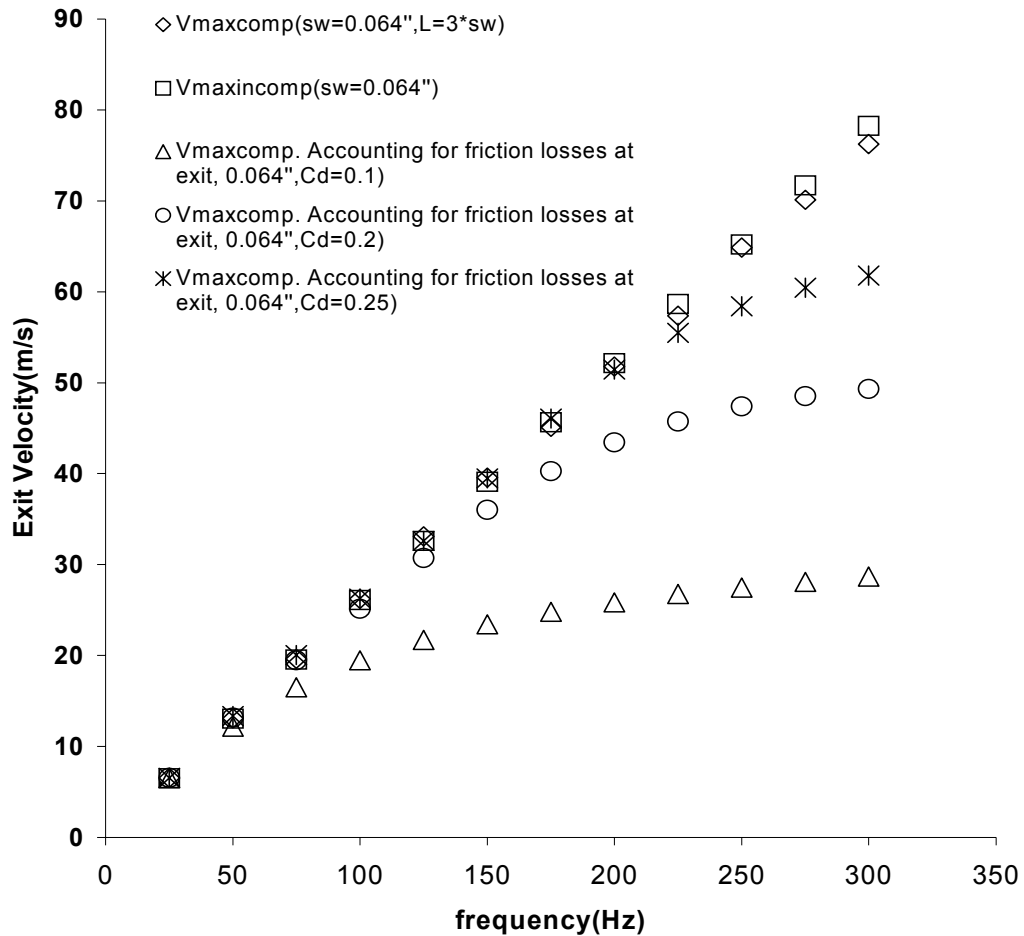


FIGURE 14. Jet exit velocity comparison between incompressible and compressible cases with and without friction losses for slot width 0.064”.

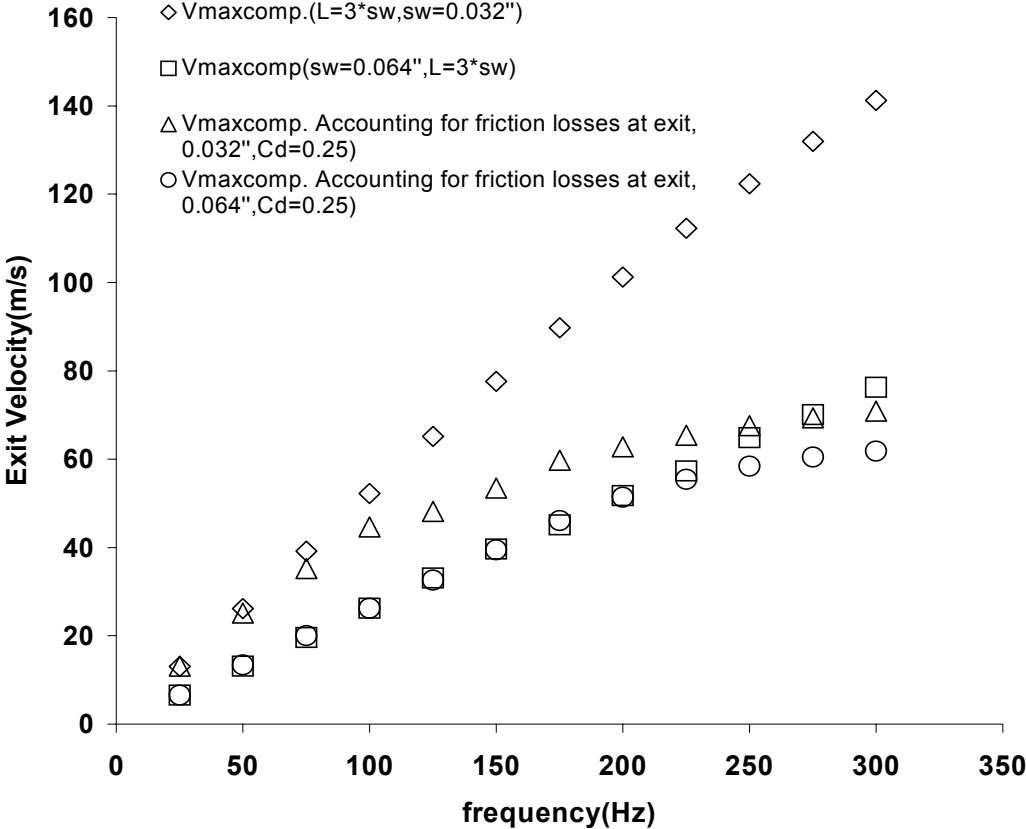


FIGURE 15. Variation of jet exit velocity with slot width for the compressible case accounting for friction losses at exit.

As stated previously, the same observation that friction and viscous effects predominate at higher frequencies than at lower frequencies is observed in Figure 14. The comparison of viscous effects between the two slot widths itself is made in Figure 16. Also, the same trend of the jet exit velocity variation with C_d is observed with the larger slot as the smaller slot. The smaller C_d values correspond to larger viscous losses and separation effects at the exit slot plane.

Figure 15 represents the variation of jet exit velocity with slot width for the compressible theoretical model without accounting for friction losses and the model accounting for friction losses at the exit. This plot assumes a C_d value of 0.25.

It can be seen from Figure 15 that the smaller slot has higher viscous losses and flow separation effects compared to the larger slot. In fact, the larger slot exhibits very little viscous effects and the exit velocity between the compressible cases with and without friction match pretty well suggesting that we should consider the large viscous/friction effects produced by a smaller slot while optimizing the design of the SJA. Also the viscous losses and flow separation effects predominate only at higher frequencies for both slots. For the smaller slot, the viscous losses start to dominate at around 100 to 125 Hz frequency whereas for the larger slot, the viscous losses start surfacing only at frequencies as high as 200 to 225 Hz.

Figure 16 represents the variation of exit velocity with cavity volume between the compressible case with and without accounting for friction losses, for a slot width 0.032 inches.

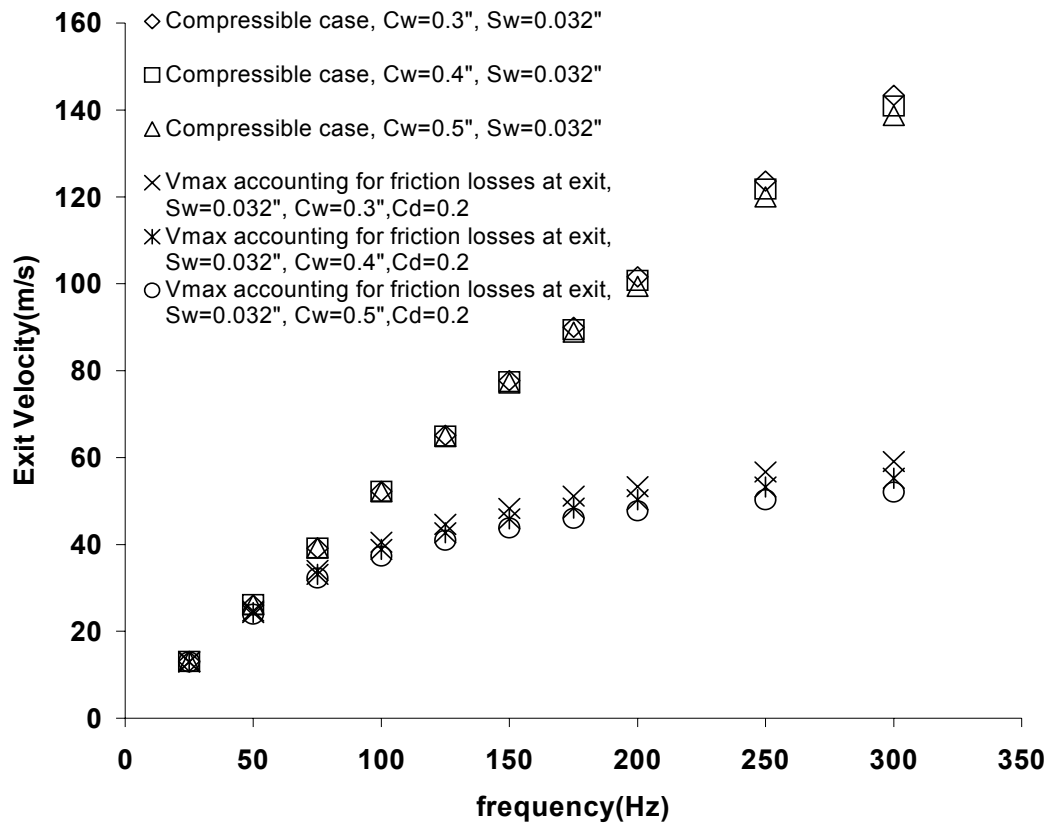


FIGURE 16. Variation of jet exit velocity with cavity volume for the compressible case with and without friction for slot width 0.032".

As observed earlier, Figure 16 suggests that an increase in cavity volume reduces the velocity in both cases. This leads us to conclude that the viscous effects / friction effects are also more predominant in the case of a larger cavity. However, it is also observed that for the smaller slot, the cavity sizes tested do not show too much variation in jet exit velocity compared with the larger slot. Also at smaller frequencies, where the flow is more incompressible, the cavity volume does not have any effects on the jet exit velocity. These factors should be considered while designing the cavity for optimal

performance of the SJA.

Figure 17 represents the variation of jet exit velocity with cavity volume between the compressible case without accounting for friction and the compressible case accounting for friction losses, for a slot width 0.064”.

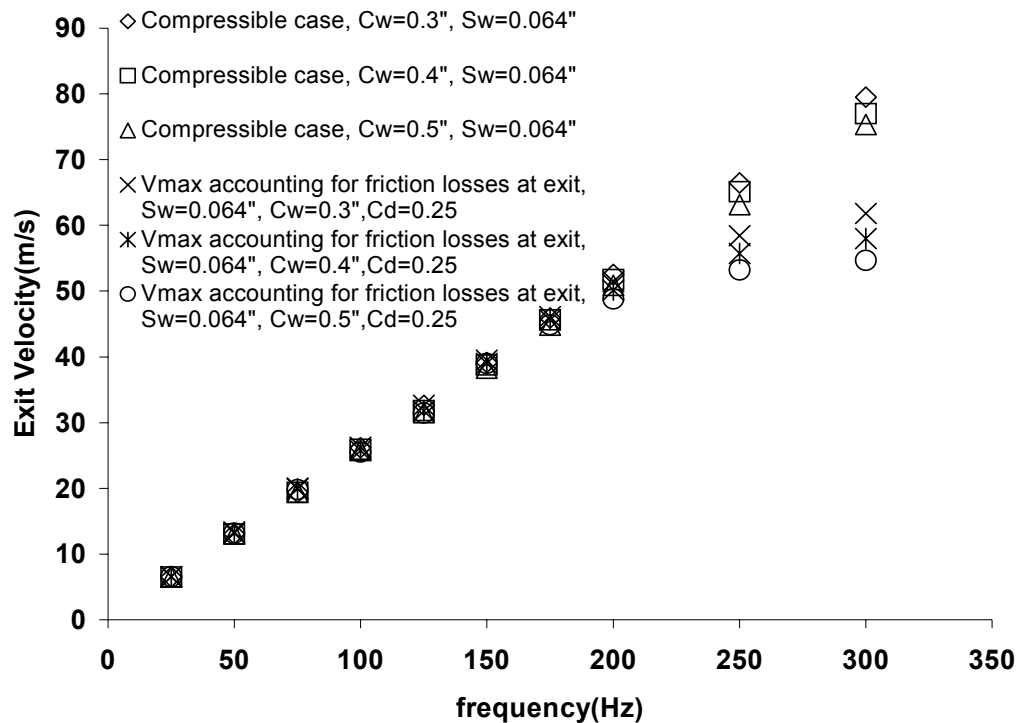


FIGURE 17. Variation of jet exit velocity with cavity volume for the compressible case with and without friction losses for slot width 0.064”.

As stated previously, the same trend is observed here. The larger cavity volume seems to show more viscous / friction effects. It should also be noted here that the larger slot shows more variation in jet exit velocity with cavity volume as compared to the

smaller slot. A correct balance between the slot size and the cavity size needs to be made with the help of these plots that would maximize the jet exit velocity and also the flow reattachment performance using the SJA.

The influence of C_d on the jet exit velocity needs to be examined further. Currently, based on the information available, it has been concluded that a C_d value of around 0.2 seems to match the theoretical compressible case velocity well with the experimental value at a slot width of 0.032 inches and a C_d value of around 0.25 seems to match the theoretical compressible case velocity well with the experimental value at a slot width of 0.064 inches.

The C_d is expected to be a function of the frequency and the geometry of the exit slot of the SJA. A more exhaustive study into the effects of the streamline curvature effects on the exit slot velocity is required to understand this phenomenon thoroughly.

The theoretical models presented above provide a good insight into the effects of compressibility and viscosity at the exit slot on the performance of the SJA. Based on these results, the SJA design has to be optimized to achieve maximum flow reattachment. The theoretical models are now validated by comparing them with hot-wire anemometer experiments performed under similar conditions. The accuracy of the current theoretical model developed in predicting the performance of any geometry/design of SJA is discussed later in this chapter.

EXPERIMENTAL STUDIES USING HOT-WIRE ANEMOMETRY

The above theoretical models to predict the compressibility effects of the jet at the slot exit need to be validated. For this purpose, hot wire anemometer experiments were performed to measure the slot exit velocity under different test conditions to compare and validate with the theoretical models. A constant current hot wire anemometer setup is used to perform the experiments. The hotwire is first calibrated using a Barocell Pressure Standard calibrator. An overheat ratio of 1.7 was used for calibration.

Three different cavity volumes and two different slot widths were used for our experiments. The inside of the cavity where the air enters the slot was smoothed to

minimize flow separation. Figures 2 and 3 represent the design of the cavity and exit slot respectively. Most previous researchers have used a circular orifice. This slot has a rectangular cross-section with a curved geometry at its end making the air gradually exit on to the wing surface tangentially and also this curvature minimizes separation effects at the exit slot.

The exit velocity is measured at the center of the exit slot. This is achieved by measuring the exit velocity at four different points along the slot width and the maximum of these velocities is taken as the velocity at the center of the slot.

The anemometer is connected to an oscilloscope and the voltage fluctuation from the anemometer is recorded through the oscilloscope and this in turn is connected through a parallel port to the computer, where the voltage data is recorded as a function of time for different frequencies of oscillation of the motor using a data acquisition board in the computer. This voltage data is then reduced to velocity data using the calibration file generated earlier.

The frequency of the motor was varied from 0 to 150 Hz in steps of 25 Hz. The motor frequencies were not steady after 150 Hz. Hence this is the maximum frequency that was tested. It should be noted here that piezo-electrically driven actuators and all other previous designs of actuators could produce only very low jet exit velocities. The one advantage that the current D/C motor-driven actuator has over the previous designs is that at higher operating frequencies, very high jet exit velocities can be generated.

The results of this experimental study are then compared with the theoretical models presented above to validate and account for the compressibility effects of the jet at the exit slot.

RESULTS AND DISCUSSION OF EXPERIMENTAL STUDY

The following section presents the results of the experimental study performed using a hot wire anemometer to study the effects of geometry and design on the performance of the SJA.

Figure 18 represents the comparison between experimental and theoretical incompressible and compressible case without accounting for friction at slot width 0.032 inches.

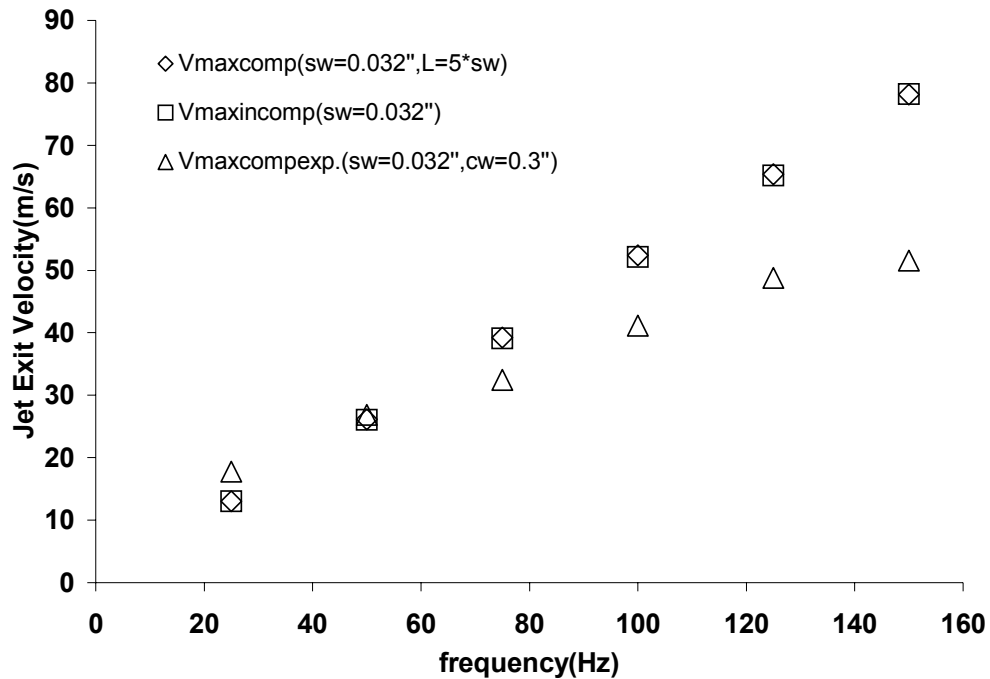


FIGURE 18. Jet exit velocity comparison between experiment and theoretical compressible case without accounting for friction losses at slot width 0.032”.

Figure 18 shows that the experimental jet exit velocity matches the theoretical case reasonably well at smaller frequencies as expected where the compressibility and the friction / viscous effects are negligible. At higher frequencies however, the friction effects predominate and need to be compared with the model that accounts for friction losses at the exit.

Figure 19 represents the comparison between experimental and theoretical incompressible and compressible cases without accounting for friction at slot width 0.064 inches.

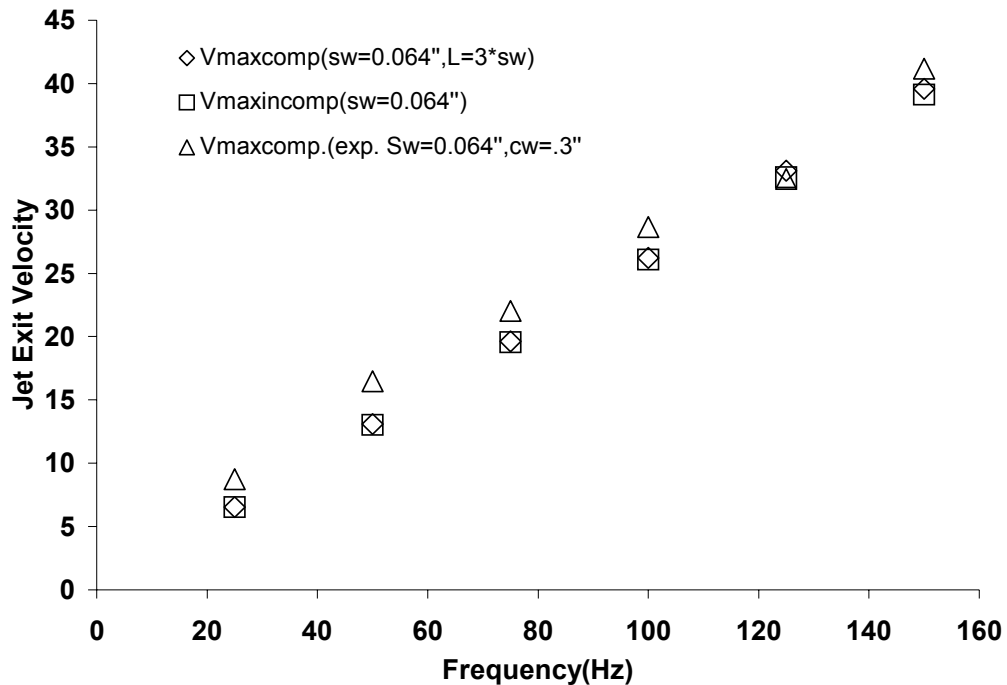


FIGURE 19. Jet exit velocity comparison between experiment and theoretical compressible case without accounting for friction losses at slot width 0.064”.

Based on Figure 19, it can be seen that the compressibility effects and friction loss effects are not too predominant for the larger slot width when compared to the smaller slot. The discrepancy of the experimental velocity being slightly higher than the theoretical compressible case may be attributed to errors involved while conducting the experiment. The hot-wire anemometer damping and inability to exactly measure at the

center of the slot may be factors that need to be considered while conducting the experiment and accounting for the discrepancies.

Figure 20 compares experimental results and theoretical compressible results with and without accounting for friction losses at exit for slot width 0.032 inches.

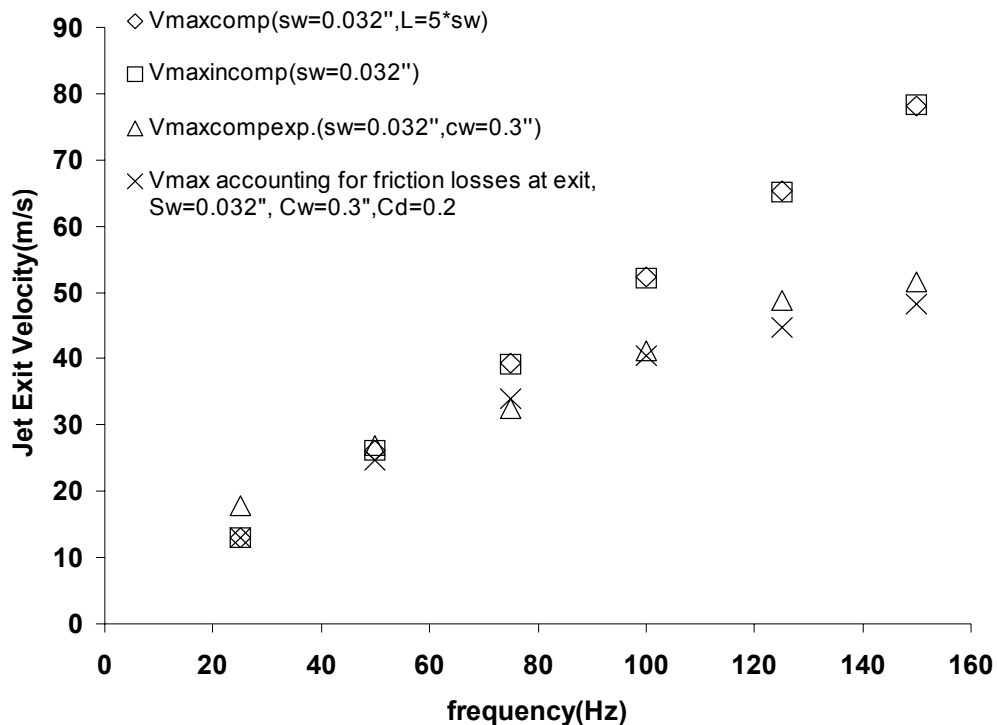


FIGURE 20. Jet exit velocity comparison between experimental and theoretical compressible cases with and without accounting for friction losses at exit for slot width 0.032”.

It can be seen from Figure 20 that a C_d value of 0.2 for the theoretical model accounting for friction losses at the exit seems to predict the exit velocity within a good accuracy of the experimental case. Further it is observed that this smaller slot shows

more friction loss / viscous effects than the larger slot, which is reproduced by the experimental results. At smaller frequencies however, the experimental jet velocity behaves similar to the incompressible velocity, as expected.

Figure 21 compares experimental results and theoretical compressible results with and without accounting for friction losses at exit for slot width 0.064 inches.

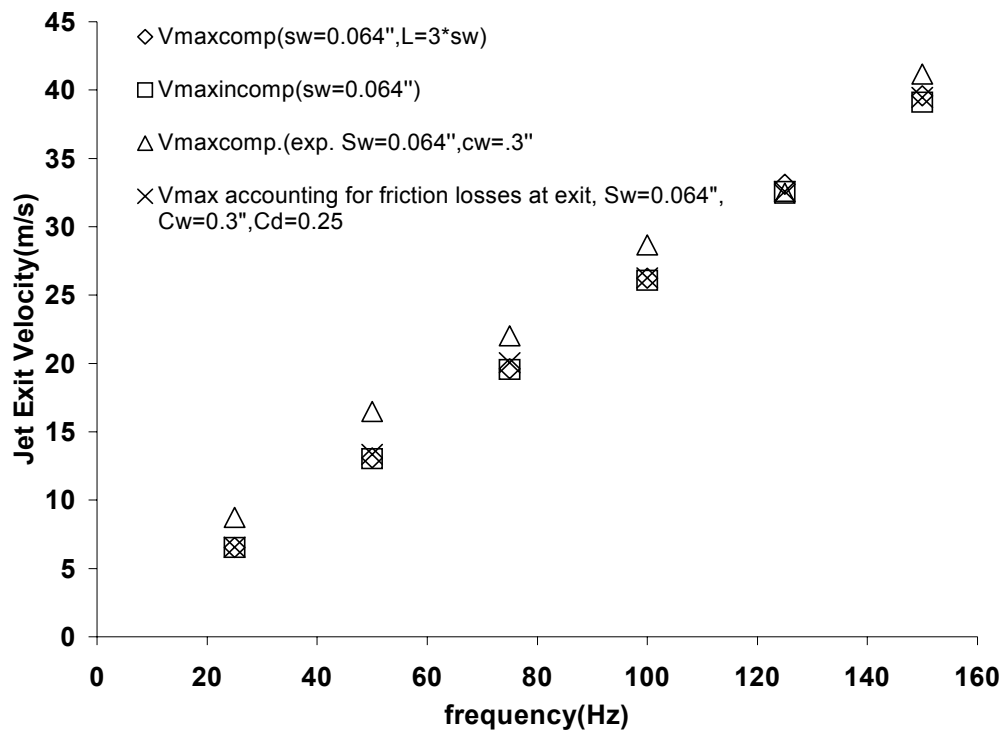


FIGURE 21. Jet exit velocity comparison between experimental and theoretical compressible cases with and without accounting for friction losses at exit for slot width 0.064".

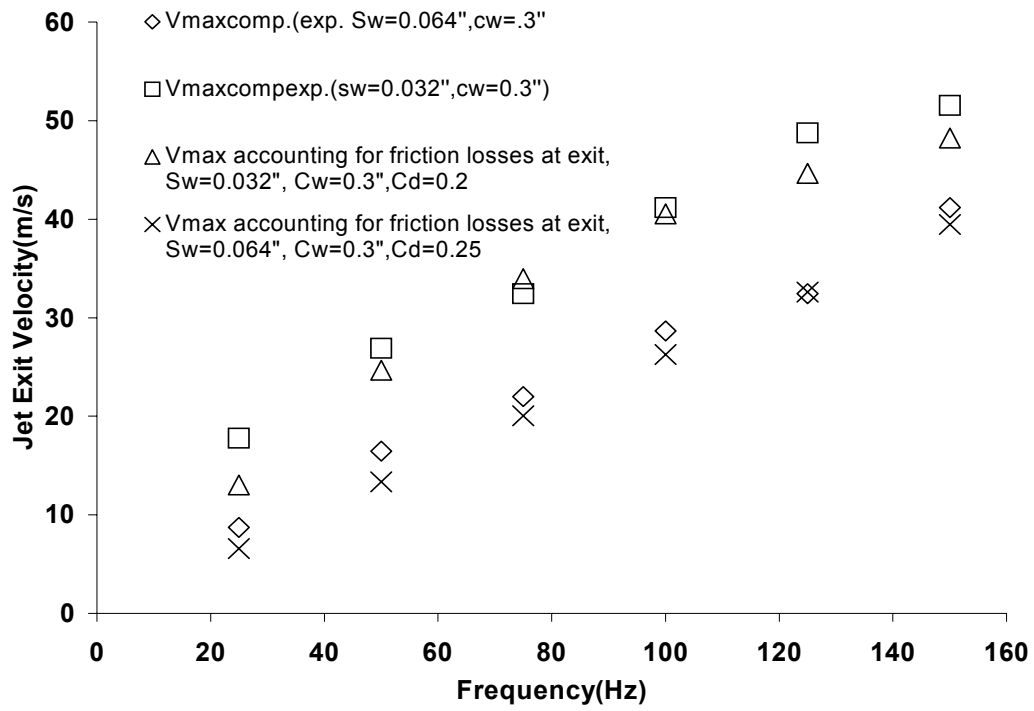


FIGURE 22. Variation of jet exit velocity with slot width for experimental study and the theoretical compressible model accounting for friction losses.

As in the previous case, the experimental velocity is compared to the theoretical model accounting for friction losses and a C_d value of 0.25 predicts the experimental velocity to a good accuracy. As stated earlier though, the compressibility and the friction losses effects are less predominant in the larger slot when compared to the smaller slot, which is proven by the experimental results too.

Figure 22 represents the variation of exit velocity with slot width for the experimental study and the theoretical model accounting for friction losses at exit.

Figure 22 shows that, as expected, both the theoretical and experimental models predict the larger slot to have a smaller velocity. Also, the smaller slot seems to exhibit more friction losses and compressibility effects when compared to the larger slot. At smaller frequencies however, both the slot widths behave very close to the incompressible case. These factors have to be considered while designing the slot geometry/size of the SJA.

Figure 23 represents the variation of exit velocity with cavity volume for both the experimental study and the theoretical compressible model accounting for friction losses at the exit for slot width 0.032 inches.

Based on Figure 23, it is seen that as predicted by the theoretical model, the higher cavity volume produces the smaller jet velocity and hence shows more compressibility effects and also shows more friction loss / viscous effects compared to the smaller cavities. This needs to be considered while designing the cavity of the SJA. At lower frequencies however, as stated earlier, the cavity volumes tested do not have much of an effect on the jet exit velocity. It should however be noted here that with the

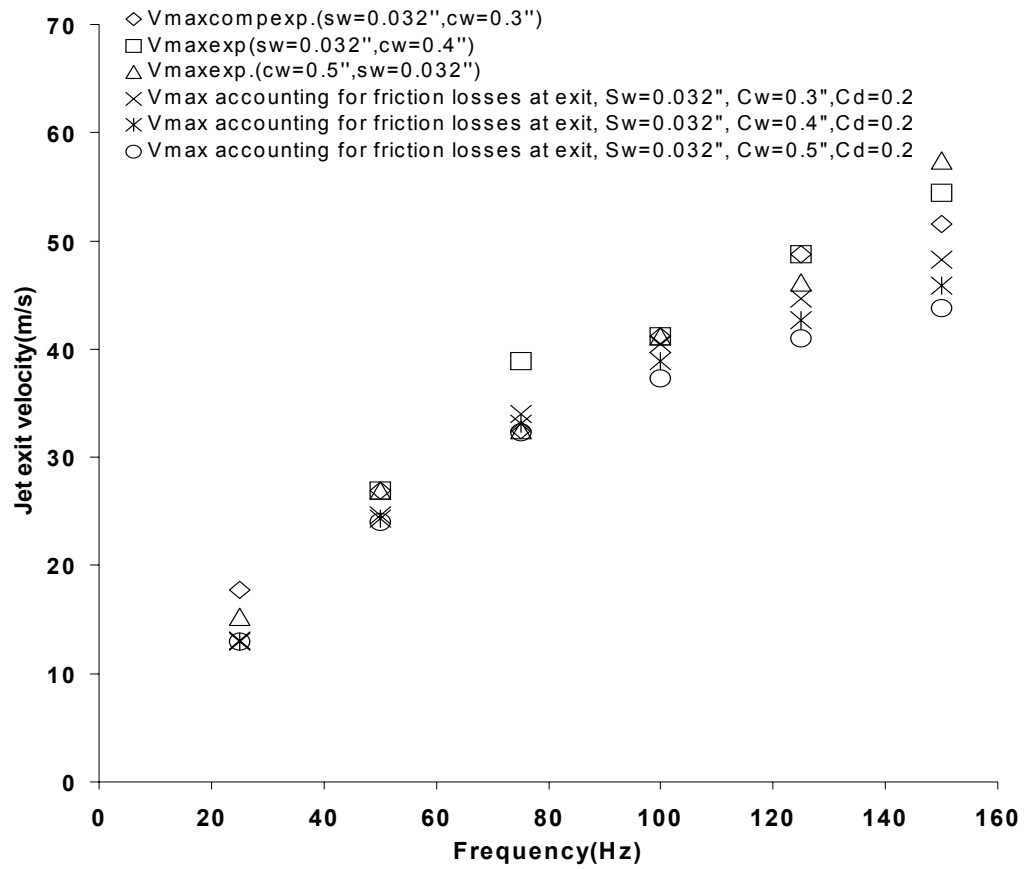


FIGURE 23. Variation of exit velocity with cavity volume for the experimental study and the theoretical compressible model accounting for friction losses for slot width 0.032".

current DC motor-driven actuator, the SJA can be operated at higher frequencies producing a higher velocity of the jet thus necessitating the need for study of cavity volume effects on the performance of the SJA.

Figure 24 represents the exit velocity variation with cavity volume between the experimental case and the theoretical compressible case accounting for friction for slot width 0.064 inches.

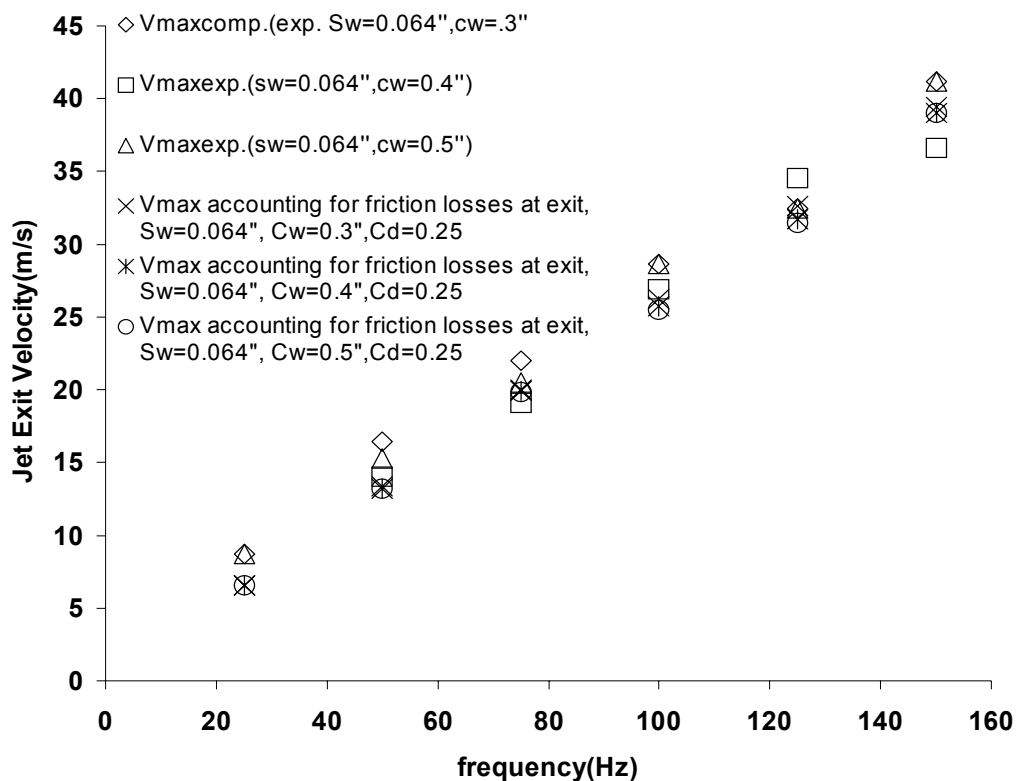


FIGURE 24. Variation of exit velocity with cavity volume for experimental study and theoretical compressible model accounting for friction for slot width 0.064".

As stated earlier, Figure 24 suggests that a larger cavity volume produces a smaller velocity as predicted by the theoretical model indicating that the smaller cavity is desirable to produce larger velocities, which achieve more efficient flow reattachment.

The above analysis should be used to optimize the design of the SJA to identify what slot width and cavity volume combination will maximize the blowing momentum coefficient to allow complete flow reattachment. Also, the geometry of the exit slot needs to be changed to see what effects different slot geometry with minimal viscous effects and separation effects would have on the exit velocity.

CONCLUSIONS

A theoretical study of the compressibility effects and the viscous losses and flow separation effects on the jet exit velocity of a DC motor-driven SJA was presented. The effects of geometry/dimensions of cavity and exit slot and other actuator parameters like the motor driving frequency on the jet exit velocity were studied using the theoretical models. Based on the results presented, the design of the exit slot and the cavity needs to be optimized and a correct combination of the two needs to be established to achieve maximum flow reattachment with minimum losses. More drastic cavity volume changes are recommended to observe better performance of the SJA. The geometry of the exit slot and the cavity need to be changed to see what effects they have on the exit velocity. Different oscillation amplitudes of the piston/cylinder will also enable us to tune the actuator frequency to match the frequency required to achieve an F^+ value of 1 which is when maximum flow reattachment has been observed to occur.

ELECTRO-ACOUSTIC MODEL OF D/C MOTOR DRIVEN SJA

INTRODUCTION

Most previous studies/research of synthetic jet actuators has focused on the design, visualization and/or measurement of synthetic jets (Crook et al., 1999; Chen et al., 2000; Crook and Wood, 2001; Gilarranz and Rediniotis, 2001). Furthermore several computational studies have also focused on fundamental aspects of these devices (Kral et al., 1997; Rizzeta et al., 1998; Mallinson et al., 2000). A proper dynamic model of the synthetic jet actuators to study the effects of geometric parameters and material dimensions and optimize the design has never been exhaustively presented. This research attempts to develop a new electro-acoustic model to predict the frequency response function of the D/C motor-driven SJA. Previous researchers have presented Lumped Element Models of Piezoelectric-Driven SJAs (Louis Cattafesta, 2002). To the author's knowledge, this is the first attempt at developing a dynamic model of a D/C motor-driven SJA. A thorough understanding and scaling of the operational characteristics of an SJA is essential to develop an optimal design for the actuator. In addition, feedback control applications require the actuator transfer function that relates the input voltage to the output property of interest (volumetric flow rate in our case).

The idea behind treating a mechanical system, as an equivalent electro-acoustic circuit is that electrical elements are a lot easier to model compared to mechanical elements. The design represents an electro-mechanical-acoustic coupled system with frequency-dependent properties determined by the device dimensions and material properties. So, each mechanical element is represented as an equivalent resistance, capacitance and inductance. The mass represents storage of kinetic energy and is modeled as an inductance. The compliance represents storage of potential energy and is modeled as a capacitance and the structural losses and frictional resistance represent a dissipation of energy and are modeled as an electric resistance. Force is modeled as a voltage and the current for the circuit is an equivalent volume velocity or flow rate.

The general principle involved in this modeling is that elements having a common effort or energy are connected in parallel and elements having the same amount

of flow rate are connected in series. A dummy voltage is then added to the circuit and represents the driving voltage of the circuit. This circuit is then analyzed and solved to generate the frequency response function, which is the ratio of the volumetric flow rate to the applied input voltage.

PHYSICAL REPRESENTATION OF ELECTRO-ACOUSTIC CIRCUIT

For a synthetic jet actuator, there are three different energy domains. They are the electrical, mechanical, and the acoustic/fluidic domain.

The motor driving voltage creates an effective acoustic pressure driving the piston into motion, which produces the jet; a part of which exits through the exit slot and the rest circulates within the cavity. This represents a conversion of the electrical energy of the D/C motor to the mechanical energy of the piston. The power associated with the D/C motor can be divided into four different parts. The main portion of this power is the useful power delivered to the piston/load (P_L). A part of the power supplied by the source voltage is dissipated as heat in the windings of the armature of the motor (P_E). Another part of the power is lost as friction in the bearings of the motor (P_F). The torque produced by the rotation of the rotor of the motor has a power associated with it (P_R) and also the torque produced by the rotation of the crank shaft/belts and the piston connecting rod also have a power associated with them (P_M). It should be noted here that P_M is a part of the power delivered to the piston/load (P_L) and need not be evaluated separately. The friction in the bearings of the motor is currently assumed to be negligible in this analysis. All of these individual powers are lumped into one single driving voltage, which is assumed to be the dummy driving voltage of this electro-acoustic circuit.

$$P_L + P_E + P_F + P_R = P_{TOTAL} \quad (32)$$

$$P_{TOTAL} = V_{AC} \cdot I \quad (33)$$

where I is the dummy current that drives this electro-acoustic circuit and is discussed below.

The motor driving the piston into motion represents a conversion from electrical to the acoustic energy domain. This conversion is accounted for using a transformer in the circuit with turns ratio ϕ_A having the units of pressure over voltage.

An ideal transformer obeys the law

$$I = Q \cdot \phi_A \quad (34)$$

where Q is the volumetric flow rate and I is the current flowing through it.

If P is the acoustic pressure term, then

$$V_{AC} = \frac{P}{\phi_A} \quad (35)$$

If Z_E and Z_A are the electric and acoustic impedances respectively of each individual element, then

$$Z_E = \frac{V_{AC}}{I} = \frac{P}{Q \cdot \phi_A^2} \quad (36)$$

$$Z_A = \frac{P}{Q} \quad (37)$$

From the above equation, we get

$$Z_E = \frac{Z_A}{\phi_A^2} \quad (38)$$

The transformer in the circuit is then included by converting all the acoustic impedances into their respective electric impedance using the above equation. Hence, the transformer is eliminated from our circuit.

V_{AC} is the input A/C voltage driving this circuit.

The source current associated with the source voltage driving the motor is given as

$$I_S = \frac{V_S}{Z_M} \quad (39)$$

The dummy A/C voltage driving this circuit is now expressed using equations (33) and (34) as

$$V_{AC} = \frac{P_{TOTAL}}{\phi_A \cdot Q} \quad (40)$$

The turns ratio ϕ_A has units of Pa/V, which is pressure per unit applied voltage. The piston oscillations have to overcome an effective acoustic pressure, which we assume in this case is the pressure created on the surface of the piston. Hence, to find out the turns ratio, we just divide the pressure on the surface of the piston by the source voltage, that drives the motor.

Using unsteady Bernoulli's equation between the surface of the piston and the exit slot plane,

$$P_P + \frac{1}{2} \cdot \rho \cdot U_P^2 = P_O + \frac{1}{2} \cdot \rho \cdot U^2 + \frac{\partial \phi_O}{\partial t} - \frac{\partial \phi_P}{\partial t} \quad (41)$$

$$\phi_A = \frac{P_P}{V_S} \quad (42)$$

Substituting for P_P from equation (41) and V_S from equation (46), we get

$$\phi_A = \frac{P_O + \frac{1}{2} \cdot \rho \cdot (U^2 - U_P^2) + \dot{U} \cdot l}{V_O \cdot \sin(\omega \cdot t)} \quad (43)$$

The piston impedance consists of an acoustic mass, which accounts for the kinetic energy of the moving mass of air and the piston mass and any other moving parts of the piston and also an acoustic resistance, which accounts for any friction losses of the moving mass of the air along the piston/cylinder lining and also the resistance/friction associated with the mechanical components of the moving parts of the piston. The piston has no compliance and hence we can quantify its displacement. Alternatively, an acoustic compliance may be included in the piston impedance, if its displacement is not specified.

A part of the jet produced by the piston oscillations exits through the exit slot and the rest circulates within the cavity. Hence the cavity impedance and the exit slot impedance are connected in parallel to one another, with the resulting impedance being in series with the piston impedance. This accounts for the flow rate Q being split between the exit slot (Q_{OUT}) and the cavity ($Q - Q_{OUT}$).

The kinetic energy of the mass of air exiting the slot is modeled as an acoustic mass, its viscous loss or dissipation is modeled as an acoustic resistance element and the exit slot discharge is also modeled as an acoustic resistance element. An acoustic compliance, to account for the potential energy stored by the mass of air in the exit slot is also included in the modeling.

The cavity contains air, which has zero mass flux. Hence it has no momentum and hence no kinetic energy. Hence, the cavity impedance consists of just an acoustic compliance, which is calculated based on the assumption that the air inside the cavity behaves like an ideal gas.

EVALUATION OF FREQUENCY RESPONSE FUNCTION

The frequency response function of the D/C motor-driven SJA is the ratio of the volumetric flow rate of air through the exit slot to the input applied voltage.

If we represent Ω as the Frequency Response Function,

$$\Omega = \frac{Q_{OUT}}{V_{AC}} \quad (44)$$

The total power associated with the D/C motor is lumped into the dummy driving voltage for the circuit, as stated earlier. Let us now try to model and quantify each of these individual powers that contribute to the driving voltage.

P_L is the useful power delivered to the piston/cylinder arrangement. This can be expressed in terms of the supply voltage, torque constant, armature resistance and motor driving frequency as

$$P_L = \frac{2.\pi.K_T.V_S.f}{R_M} - \frac{4.K_T^2.\pi^2.f^2}{R_M} \quad (45)$$

The source voltage V_S is assumed to be a sinusoidal voltage which would then yield

$$V_S = V_O.\sin(\omega.t) \quad (46)$$

V_O is the amplitude of the source voltage in the above equation.

The torque constant and armature resistance are specific to a D/C motor and for the current D/C motor used to drive the SJA, these constants and other characteristics are given in Table 4.

Motor Characteristic	Value
Motor Manufacturer	AstroFlight Inc.
Motor name	Cobalt-40
Armature Winding Resistance (R_M)	0.041 Ω
Torque constant (K_T)	0.99 in-oz/amp
No Load amps	5 amps
Power	1000 W
Motor Efficiency	80 %
Motor Length	2.75 in.
Motor Diameter	1.62 in.
Motor Weight	12 oz
Shaft Diameter	0.25 in.

TABLE 4. Characteristics of Astro Cobalt Marine Racing D/C motor driving the SJA.

P_E is the electric dissipation in the armature windings of the motor. This is expressed in terms of the armature winding resistance and the supply voltage as

$$P_E = \frac{V_S^2}{R_M} = \frac{V_O^2 \cdot \sin^2(\omega t)}{R_M} \quad (47)$$

P_R is the power associated with the rotational inertia of the rotor of the motor. This can be expressed as

$$P_R = \frac{d}{dt} \left(\frac{1}{2} \cdot I_R \cdot \omega^2 \right) = I_R \cdot \omega \cdot \frac{d\omega}{dt} \quad (48)$$

P_F represents the power associated with the friction losses in the bearings of the motor. At present, we do not have too much knowledge about this and also for inline engine motors, it is assumed to be negligible. Hence, for our analysis, we assume P_F to be zero.

P_M represents the power associated with the torque produced by the rotation of the crankshaft disk, crankshaft pins and belts and the connecting rod.

Figures 25, 26, 27 and 28 represent the individual designs of the crankshaft disk, crankshaft end, crankshaft section and the connecting rod.

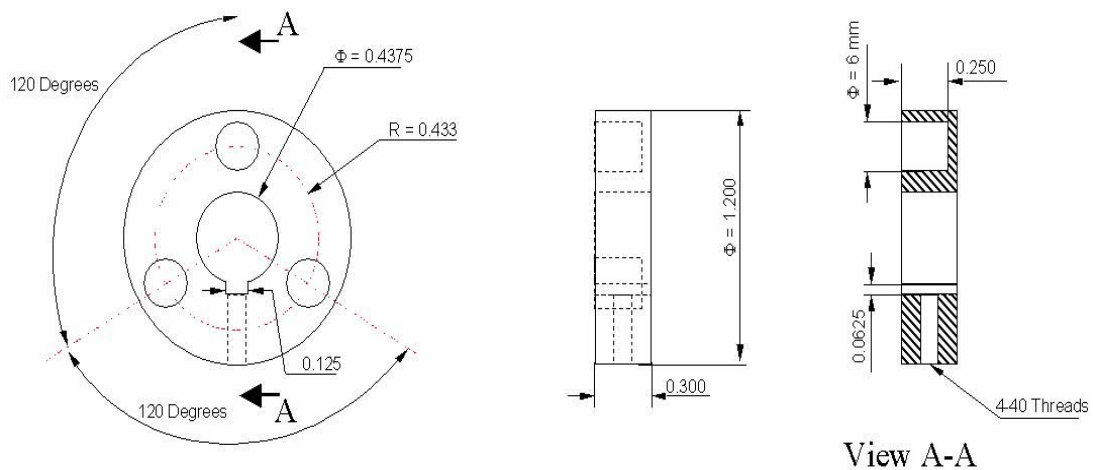


FIGURE 25. Crankshaft disk design.

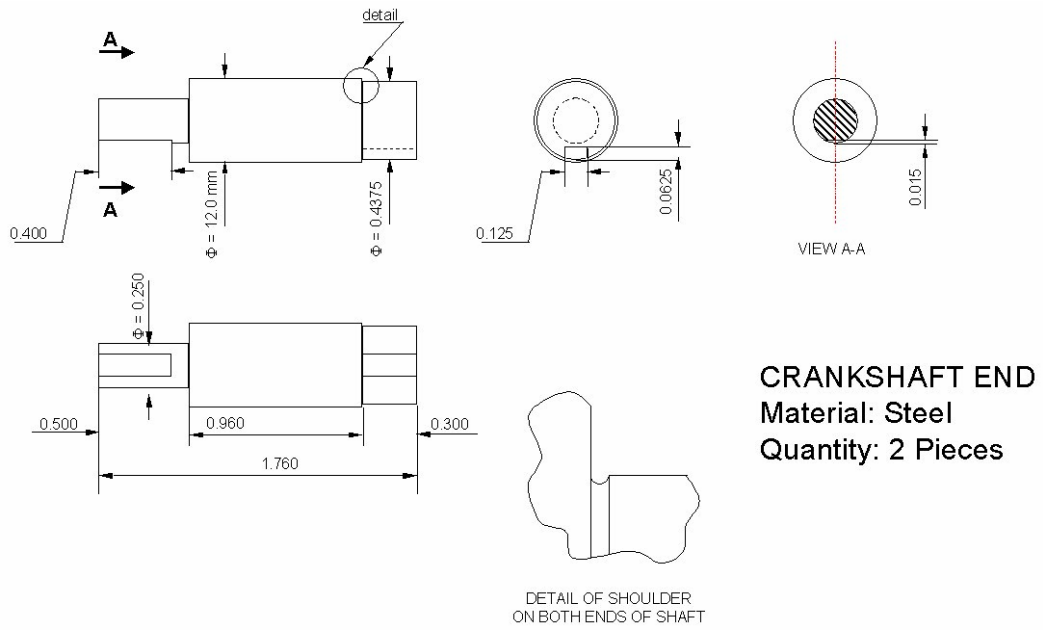


FIGURE 26. Crankshaft end design.

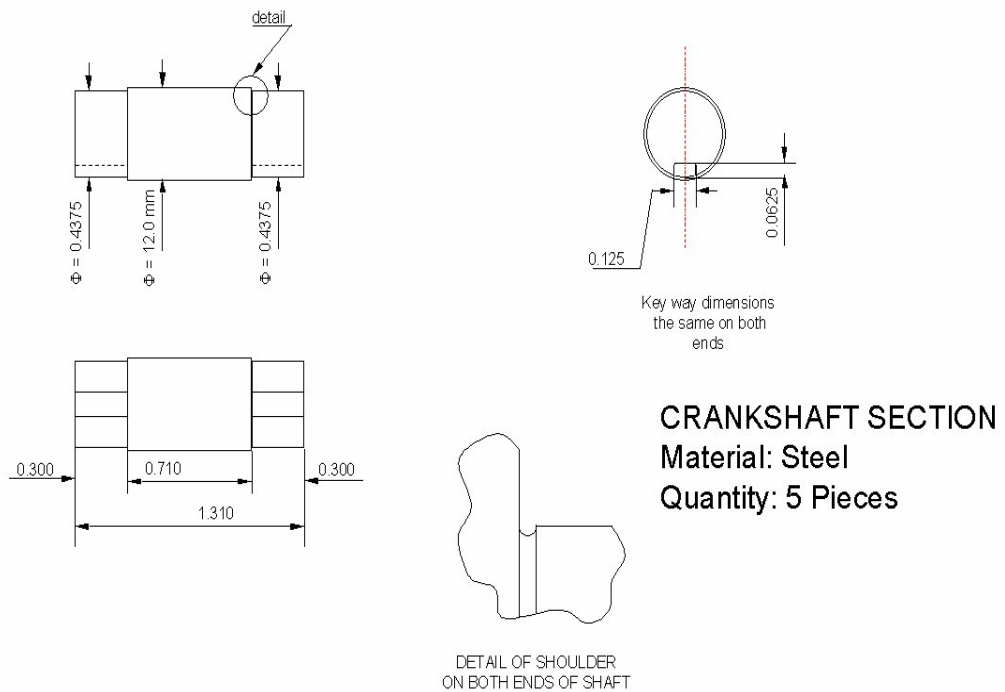


FIGURE 27. Crankshaft section design.

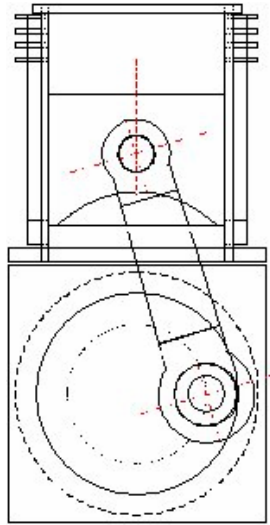


FIGURE 28. Connecting rod design.

Figures 25 to 28 are used to evaluate the moment of inertia of the crankshaft about the axis of rotation, which is also shown in the figures. This enables us to calculate the rotational kinetic energy and hence the power associated with this rotation. Hence P_M can now be expressed as

$$P_M = \frac{d}{dt} \left(\frac{1}{2} I_M \cdot \omega^2 \right) = I_M \cdot \omega \cdot \frac{d\omega}{dt} \quad (49)$$

Substituting for each of these individual power values into equation (40) yields the dummy voltage that drives this electro-acoustic circuit.

The volumetric flow rate through the exit slot of the SJA can be expressed as

$$Q_{OUT} = U \cdot A_N = U \cdot S_W \cdot S_L \quad (50)$$

Now substituting equations (40) and (50) in equation (44), we get an expression for the frequency response function as,

$$\Omega = \frac{U \cdot S_W \cdot S_L \cdot \phi_A \cdot Q}{P_{TOTAL}} \quad (51)$$

Figure 29 now gives the circuit of the electro-acoustic model used to evaluate the performance of the SJA.

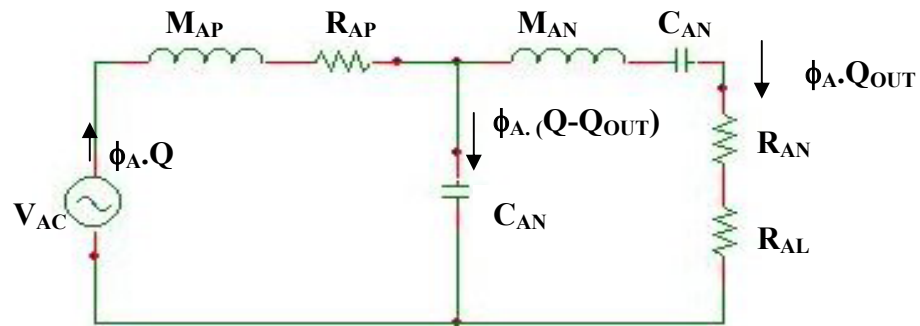


FIGURE 29. Electro-acoustic model circuit of DC motor driven SJA.

Subscript A represents acoustic domain and subscript E represents electric domain. Subscript P indicates piston/cylinder terms, subscript M indicates motor terms, subscript C indicates cavity terms and subscript N indicates exit slot/neck terms. Q_{OUT} is the volumetric flow rate of air through the exit slot of the SJA and V_{AC} is the applied input voltage to the circuit. Because a viscous resistance element has been included in the exit slot impedance, this model takes into account both viscous and inviscid flow conditions. Setting $R_{AL} = 0$ would mean that the viscous effects of the air at the exit slot plane have been neglected.

Figure 30 represents a simpler form of the circuit in Figure 21 to analyze the frequency response function from the circuit.

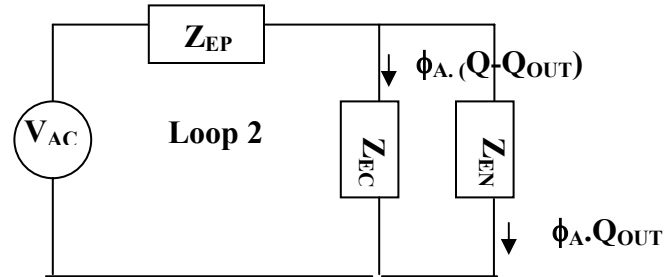


FIGURE 30. Box circuit of the electro-acoustic model of DC motor driven SJA.

Equating voltages along Loop 1 (outer loop),

$$\phi_A \cdot Q_{OUT} \cdot Z_{EN} = \phi_A \cdot (Q - Q_{OUT}) \cdot Z_{EC} \quad (52)$$

Rearranging we get,

$$Q = \frac{Q_{OUT} \cdot (Z_{EC} + Z_{EN})}{Z_{EC}} \quad (53)$$

Equating voltages along Loop 2,

$$V_{AC} = \phi_A \cdot Q \cdot Z_{EP} + \phi_A \cdot Q \cdot Z_{EFF} \quad (54)$$

$$Z_{EFF} = \frac{Z_{EC} \cdot Z_{EN}}{Z_{EC} + Z_{EN}} \quad (55)$$

Rearranging these terms, we get

$$V_{AC} = \phi_A \cdot Q \left[Z_{EP} + \frac{Z_{EC} \cdot Z_{EN}}{Z_{EC} + Z_{EN}} \right] \quad (56)$$

Eliminating Q using equations (53) and (56), we get an expression for the frequency response function, Ω ,

$$\Omega = \frac{Q_{OUT}}{V_{AC}} = \frac{Z_{EC}}{\phi_A \cdot (Z_{EP} \cdot Z_{EC} + Z_{EP} \cdot Z_{EN} + Z_{EN} \cdot Z_{EC})} \quad (57)$$

Each of this individual impedance is now given by

$$Z_{EP} = \frac{M_{AP} \cdot f + R_{AP}}{\phi_A^2} \quad (58)$$

$$Z_{EC} = \frac{1}{C_{AC} \cdot f \cdot \phi_A^2} \quad (59)$$

$$Z_{EN} = \frac{M_{AN} \cdot f + R_{AN} + R_{AL} + \frac{1}{C_{AN} \cdot f}}{\phi_A^2} \quad (60)$$

Subscript E in each of these impedance terms means that the acoustic impedances have been converted to their respective electrical ones by using equation (38).

We substitute for the impedance values from equations (58), (59), and (60) in equation (57) and introduce these new constants to simplify the expression.

$$A_1 = C_{AN} \cdot (R_{AP} + R_{AN} + R_{AL}) + C_{AC} \cdot R_{AP} \quad (61)$$

$$A_2 = C_{AC} \cdot C_{AN} \cdot R_{AP} \cdot (R_{AN} + R_{AL}) + C_{AN} \cdot (M_{AP} + M_{AN}) + C_{AC} \cdot M_{AP} \quad (62)$$

$$A_3 = C_{AC} \cdot C_{AN} \cdot (R_{AP} \cdot M_{AN} + M_{AP} \cdot R_{AN} + M_{AP} \cdot R_{AL}) \quad (63)$$

$$A_4 = C_{AC} \cdot C_{AN} \cdot M_{AP} \cdot M_{AN} \quad (64)$$

The frequency response function is now expressed as

$$\Omega = \frac{Q_{OUT}}{V_{AC}} = \frac{\phi_A \cdot C_{AN} \cdot f}{(1 + A_1 \cdot f + A_2 \cdot f^2 + A_3 \cdot f^3 + A_4 \cdot f^4)} \quad (65)$$

DETERMINATION OF IMPEDANCES IN CIRCUIT

This section analyzes and examines each impedance qualitatively and quantitatively, concentrating on what each impedance physically represents.

Piston terms

The piston oscillations are modeled as an equivalent acoustic mass (M_{AP}) and an acoustic resistance (R_{AP}).

The acoustic mass consists of two components, the mass of the air moving with the piston and the mass of the piston itself and any other moving parts of the piston. M_{APair} is a measure of the kinetic energy of the mass of the air moving with the piston

and $M_{APpiston}$ is a measure of the kinetic energy of the piston and any other moving parts of the piston. The air moving with the piston is modeled assuming fully developed pipe flow. We equate the kinetic energies of the acoustic mass and the actual mass of the air, to get an expression for the acoustic mass of the air moving with the piston. This assumption of Hagen-Poiseuille flow for the air moving with the piston is valid at low frequencies, where the Stokes number is low.

$$\frac{1}{2} M_{APair} Q^2 = \frac{1}{2} \int_0^{\frac{p_d}{2}} \rho(P_S - x)(Area)(velocity)^2 = \frac{1}{2} \rho(P_S - x) \int_0^{\frac{p_d}{2}} \left[U_P \left(1 - \frac{4r^2}{p_d^2} \right) \right]^2 2\pi r dr \quad (66)$$

In the above expression, P_S represents the stroke of the piston and U_P is the piston velocity, which is obtained from equation (4). The displacement of the piston at any instant of time is x from equation (3). The velocity profile used in the above equation is for fully developed pipe flow, assuming the air moving with the piston/cylinder is equivalent to the air moving in a pipe whose diameter is same as the diameter of the piston cylinder.

Evaluating the integral and simplifying the expression, we get

$$M_{APair} = \frac{\rho(P_S - x)}{3A_p} \quad (67)$$

At higher frequencies however, the Stokes number is larger, and hence the assumption of the Hagen-Poiseuille flow is no longer valid and the air moving with the piston has to be modeled as a case of pipe flow due to an oscillating pressure gradient. The solution to this problem is given in terms of the Bessel function and is difficult to evaluate analytically. The discussion of this problem is given in White (1974).

We shall however use just the results of that discussion here without giving details on how to arrive at this equation. The series approximation for the Bessel's functions has been used to obtain a simpler equation for the velocity profile and higher order terms of very small magnitude have been neglected.

We introduce the following definitions for this analysis:

$$\omega^* = \frac{\omega \cdot p_d^2}{4\nu} \quad (68)$$

where ν is the kinematic viscosity of air.

$$r^* = \frac{2.r}{p_d} \quad (69)$$

$$B = (1 - r^*) \cdot \sqrt{\frac{\omega^*}{2}} \quad (70)$$

Using the above definitions, the velocity profile of the air moving with the piston is then given as,

$$U = \frac{4.U_P}{\omega^*} \left[\sin(\omega.t) - \frac{e^{-B}}{\sqrt{r^*}} \cdot \sin(\omega.t - B) \right] \quad (71)$$

An order of magnitude analysis for each of the individual circuit impedances is performed later in this section to compare the contribution of each impedance to the model and impedances that are very small compared to the other ones are neglected. For this purpose, the impedance evaluation is carried out at the maximum velocity of the device under consideration, which is assumed to be the worst case under which the contribution of that particular impedance term is maximum. To achieve this, the time dependence in the above equation is eliminated by evaluating the time at which the velocity reaches its maximum value and substituting it in the equation.

This maximum velocity is found to occur at

$$\tan(\omega.t) = \frac{1 - \frac{e^{-B}}{\sqrt{r^*}} \cdot \cos B}{\frac{e^{-B}}{\sqrt{r^*}} \cdot \sin B} \quad (72)$$

Substituting for $\sin(\omega.t)$ and $\sin(\omega.t-B)$ from equation (72) into equation (71), we get

$$U = \frac{4.U_P}{\omega^*} \left[\sqrt{1 + \frac{e^{-2B}}{r^*} - \frac{2.e^{-B}}{\sqrt{r^*}} \cdot \cos B} \right] \quad (73)$$

The above velocity profile from equation (73) is used for the order of magnitude analysis.

Under normal conditions, using equation (71) for the velocity profile of the air moving with the piston, and equating the kinetic energies of the acoustic mass and the actual mass of the air using equation (66), the acoustic mass of the air moving with the piston is calculated as,

$$M_{APair} = \frac{\rho(P_S - x)}{A_p^2} \int_0^{\frac{p_d}{2}} \frac{16}{(\omega^*)^2} \left[\sin(\omega t) - \frac{e^{-B}}{\sqrt{r^*}} \cdot \sin(\omega t - B) \right] 2\pi r \cdot dr \quad (74)$$

The above integral is solved numerically using Simpson's rule.

The acoustic mass of the piston and its moving parts is also obtained by equating the kinetic energies of the acoustic mass and the actual mass of the piston and its moving parts as described earlier for the air moving with the piston.

$$\frac{1}{2} \cdot M_{APpiston} \cdot Q^2 = \frac{1}{2} \cdot M_p \cdot U_p^2 \quad (75)$$

M_p is the mass of the piston and its moving parts and is measured using a weight balance.

Simplifying equation (75), we get

$$M_{APpiston} = \frac{M_p}{A_p^2} \quad (76)$$

Hence the total acoustic mass of the piston terms at low frequencies is given as

$$M_{AP} = \frac{\rho \cdot (P_S - x)}{3 \cdot A_p} + \frac{M_p}{A_p^2} \quad (77)$$

The acoustic resistance of the piston is also comprised of two parts. R_{APair} represents the resistance or friction of the mass of the air moving with the piston along the piston/cylinder walls and $R_{APpiston}$ represents the resistance associated with the mechanical components of the moving parts of the piston. The resistance of the air moving with the piston is calculated assuming fully developed pipe flow.

$$R_{APair} = \frac{\Delta p_{OUT}}{Q_{OUT}} = \frac{8 \cdot \mu \cdot (P_S - x)}{\pi \cdot \left(\frac{p_d}{2}\right)^4} \quad (78)$$

However, as stated earlier, the assumption of Hagen-Poiseuille flow is valid only at low frequencies, where the Stokes number is close to zero. At higher frequencies, we use the pipe flow due to oscillating pressure gradient.

$$R_{APair} = \frac{\Delta p}{Q} = \frac{8 \cdot \mu \cdot U_p}{p_d \cdot Q} \quad (79)$$

where Q is calculated using the velocity profile for this case from equation (71) as

$$Q = \int_0^{\frac{p_d}{2}} \frac{4 \cdot U_p}{\omega^*} \left[\sin(\omega \cdot t) - \frac{e^{-B}}{\sqrt{r^*}} \cdot \sin(\omega \cdot t - B) \right] \cdot 2\pi r \cdot dr \quad (80)$$

The above integral is again solved using numerical methods and substituted into (79) to get the acoustic resistance of the air moving with the piston.

To calculate the resistance of the mechanical components of the piston, we equate the force experienced at the surface of the piston to the rate of change of linear momentum of the mechanical components of the piston.

$$F_{MP} = M_p \cdot \frac{dV}{dt} = 2 \cdot \pi \cdot f \cdot M_p \cdot U_p \quad (81)$$

Hence,

$$R_{APpiston} = \frac{F_{MP}}{Q \cdot A_p} \quad (82)$$

Substituting (81) in (82), we get

$$R_{APpiston} = \frac{2 \cdot M_p \cdot \pi \cdot f}{A_p^2} \quad (83)$$

Hence, the total acoustic resistance of the piston terms at low frequencies is given as

$$R_{AP} = \frac{8 \cdot \mu \cdot (P_s - x)}{\pi \left(\frac{p_d}{2} \right)^4} + \frac{2 \cdot M_p \cdot \pi \cdot f}{A_p^2} \quad (84)$$

Also, as mentioned earlier, the piston does not have any compliance.

Cavity terms

The air in the cavity is modeled as an acoustic compliance. It has no momentum and hence the kinetic energy associated with the mass of air in the cavity is zero and hence we do not associate an acoustic mass with the cavity.

We assume the air inside the cavity behaves like an ideal gas, which would give

$$C_{AC} = \frac{V_C}{\rho \cdot c_s^2} \quad (85)$$

In the above expression, c represents the speed of sound in air.

The frictional resistance inside the cavity is negligible. Hence, we do not associate an acoustic resistance with the cavity.

Neck / Exit slot terms

The air in the exit slot is modeled as an acoustic mass (M_{AN}), an acoustic resistance (R_{AN}) and an acoustic compliance (C_{AN}). Alternatively, we could add another resistance, R_{AL} that represents the viscous losses in the exit slot. Setting $R_{AL} = 0$ would then represent inviscid flow at the exit.

The acoustic mass is a measure of the kinetic energy of the air in the exit slot. The air in the exit slot is modeled assuming flow between infinite plates, because the exit slot currently studied has a rectangular cross-section. We equate the kinetic energies of the acoustic mass and the actual mass of the air, to get an expression for the acoustic mass of the air in the exit neck. This Poiseuille flow velocity profile assumption is valid only at low frequencies, where the Stokes number is close to zero.

$$\frac{1}{2} \cdot M_{AN} \cdot Q_{OUT}^2 = \frac{1}{2} \cdot \rho \cdot L \cdot \int_0^{s_w/2} \left[U \left(1 - \frac{4 \cdot x^2}{s_w^2} \right) \right]^2 \cdot S_L \cdot dx \quad (86)$$

The acceleration length L of the exit slot plane is assumed to vary linearly with slot width. In case of smaller slots, the air in the exit is expected to have a larger velocity and accelerate faster. Hence the slope of the acceleration length, assumed to vary linearly with the slot width, is larger. In case of larger slots, with the exit velocity and acceleration of the air being lesser, the slope of the acceleration length is smaller.

Evaluating the integral and simplifying the expression, the acoustic mass at low frequencies is expressed as

$$M_{AN} = \frac{4 \cdot \rho \cdot L}{15 \cdot A_N} \quad (87)$$

At higher frequencies however, where the Stokes number cannot be neglected, we model the mass of the air in the exit slot as an oscillating fluid between parallel plates, which is the classic case known as the Stokes second problem after a celebrated paper by Stokes (1851).

The discussion of this problem is done in White (1974) and we present just the results here. The velocity profile for the above case is given as

$$u = U \cdot \cos(\omega t) - U \cdot e^{-\eta} \cdot \cos(\omega t - \eta) \quad (88)$$

$$\eta = x \cdot \sqrt{\frac{\omega}{2 \cdot \nu}} \quad (89)$$

Here x is measured from the center of the exit slot and hence, varies between $-S_W/2$ and $+S_W/2$.

As stated earlier, in order to carry out the order of magnitude analysis, the time dependence in the above equation is eliminated by evaluating the time at which the above velocity reaches its maximum value and substituting it in the equation. This condition is expected to produce the maximum impedance value, which if still small can be neglected in the model in comparison to other impedances.

The maximum velocity occurs at

$$\tan(\omega t) = \frac{e^{-\eta} \cdot \sin \eta}{e^{-\eta} \cdot \cos \eta - 1} \quad (90)$$

Substituting for $\cos(\omega t)$ and $\cos(\omega t - \eta)$ from equation (90) into (88), the velocity profile for the order of magnitude analysis is given as,

$$u = U \cdot \sqrt{1 + e^{-2\eta} - 2 \cdot e^{-\eta} \cdot \cos \eta} \quad (91)$$

Under normal conditions, equating the kinetic energies of the acoustic mass of air in the exit slot and the actual mass of the air in the exit slot using the velocity profile from equation (88), we get

$$M_{AN} = \frac{\rho \cdot L \cdot S_L}{A_N^2} \cdot \int_{-\frac{S_W}{2}}^{\frac{S_W}{2}} [\cos(\omega t) - e^{-\eta} \cdot \cos(\omega t - \eta)]^2 \cdot dx \quad (92)$$

The above integral for M_{AN} is difficult to solve analytically and hence Simpson's numerical methods are used to evaluate the acoustic mass of air in the exit slot neck.

The acoustic resistance of the neck to account for the exit slot discharge is modeled as a generalized Bernoulli flow meter (McCormick, 2000 and White, 1979).

$$R_{AN} = \frac{\frac{1}{2} \cdot K_D \cdot \rho \cdot U}{A_N} \quad (93)$$

Here, K_D is the jet dump loss coefficient associated with the exit slot discharge and the 0.5 in the expression is introduced to account for the fact that discharge at the exit occurs only during one half of the jet cycle. A jet dump loss value of 0.75 is assumed for this model, which seems to minimize the losses (McCormick, 2000).

The resistance to account for the viscous effects at the exit slot can be modeled again, assuming flat plate theory for the air moving at the exit, the cross-section of the exit slot being rectangular. The viscous dissipation at the exit is modeled in terms of the surface resistance, R_S , which depends on the viscosity and density of air and the frequency of the motor (Uno Ingard, 1953).

$$R_S = \sqrt{\frac{\mu \cdot \rho \cdot \omega}{2}} \quad (94)$$

Then the viscous dissipation is given as (Uno Ingard, 1953)

$$R_{AL} = \frac{1}{2} \cdot \int_s R_S \cdot U_s^2 \cdot ds \quad (95)$$

U_s is the velocity profile of the air in the exit slot which is modeled using flow between parallel plates as

$$U_s = U \cdot \left(1 - \frac{4 \cdot x^2}{S_W^2}\right) \quad (96)$$

Substituting for equations (96) and (94) in equation (95), we get the viscous dissipation as,

$$R_{AL} = \frac{1}{2} \cdot \int_0^{S_w/2} R_s \left[U \cdot \left(1 - 4 \cdot \frac{x^2}{S_w^2} \right) \right]^2 \cdot S_L \cdot dx \quad (97)$$

Evaluating the integral and simplifying the expression, we get

$$R_{AL} = \frac{2 \cdot R_s \cdot A_N \cdot U^2}{15} \quad (98)$$

As stated earlier, the assumption of flow between parallel plates is valid only at low frequencies, where the Stokes number is close to zero. At higher frequencies, we use the Stokes second problem as stated before and using the velocity profile from equation (88), the viscous resistance of the air in the exit slot is given as,

$$R_{AL} = \frac{1}{2} \cdot \int_{-\frac{S_w}{2}}^{\frac{S_w}{2}} R_s \cdot U^2 \cdot [\cos(\omega t) - e^{-\eta} \cdot \cos(\omega t - \eta)]^2 \cdot S_L \cdot dx \quad (99)$$

The above integral is again evaluated using Simpson's numerical methods to calculate the viscous resistance of the air in the exit slot neck.

The acoustic compliance of the air in the exit slot is again evaluated assuming that the air at the exit slot also behaves like an ideal gas giving

$$C_{AN} = \frac{V_N}{\rho \cdot c^2} \quad (100)$$

The volume of the exit slot, V_N is got as

$$V_N = A_N \cdot L \quad (101)$$

Substituting these impedance values into equations (61)-(64) yields the constants A1, A2, A3 and A4, which enable us to evaluate the frequency response function from equation (65).

Equations (51) and (65) are two different expressions for the frequency response function in terms of the frequency of the motor and the only unknown, the jet exit velocity U. Equating these two expressions yields an equation for the jet exit velocity in terms of the frequency of the motor. All of the individual impedances are frequency-dependent parameters and some of them also depend on the jet exit velocity, which is the unknown variable being studied in this analysis. The variation of jet exit velocity with

motor frequency is now analyzed using this model. The effects of geometric parameters of the actuator on the jet exit velocity are also analyzed using this model.

The following table lists the different geometric parameters of the SJA that were tested with this model.

Piston Diameter (inches)	Piston Stroke (inches)	Exit Slot Width (inches)	Exit Slot Length (inches)	Cavity Width (inches)
0.906	0.811	0.032	2.5	0.3
0.906	0.811	0.032	2.5	0.4
0.906	0.811	0.032	2.5	0.5
0.906	0.811	0.064	2.5	0.3
0.906	0.811	0.064	2.5	0.4
0.906	0.811	0.064	2.5	0.5

TABLE 5. Different geometric parameters of SJA tested using electro-acoustic model.

RESULTS AND DISCUSSION OF EFFECTS OF GEOMETRIC PARAMETERS ON ELECTRO-ACOUSTIC MODEL

This section presents the results and discussion of the electro-acoustic model of the DC motor driven SJA. Let us first examine the variation of the impedances with the motor frequency.

Order of magnitude analysis for the impedances

The analysis of the impedances in the electro acoustic model suggests that some of the impedances are complex and involve a tedious process of evaluation. In order to simplify our model and ease our analysis, an order of magnitude analysis is performed for all of the above impedances. This would enable us to neglect those impedances

which are very small in magnitude when compared to the other ones and do not contribute much to the model. The time dependence in all of the impedances is eliminated to perform this analysis by considering the amplitude of individual impedance.

It is observed that the compliance of the cavity and the exit slot are constants with respect to frequency of oscillation of the motor.

Figure 31 represents the frequency variation of the acoustic mass of the air moving with the piston.

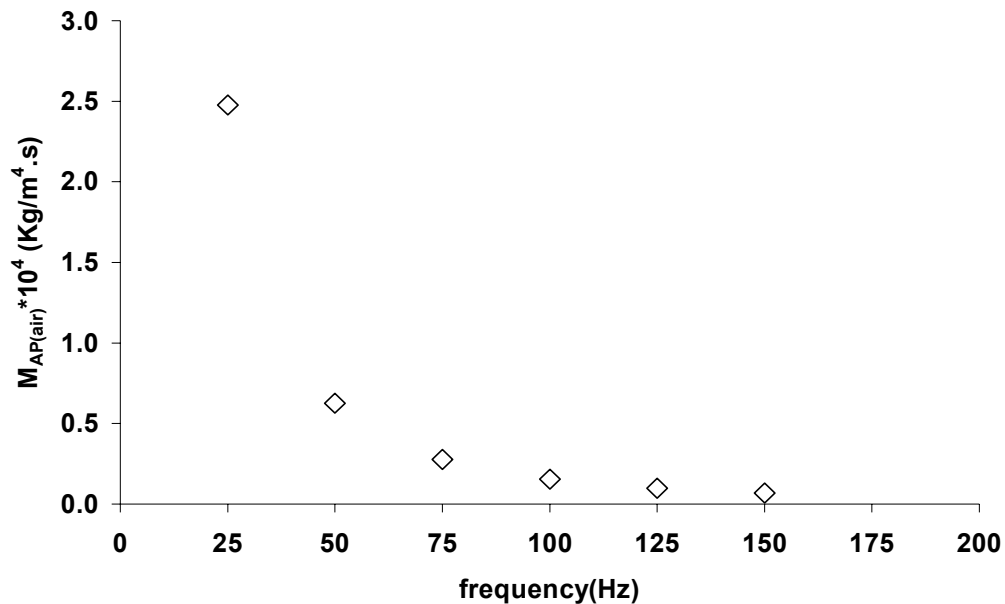


FIGURE 31. Frequency dependence of acoustic mass of air moving the piston.

The acoustic mass of the air moving with the piston seems to decrease exponentially with increasing motor frequency. At higher frequencies, the acoustic mass of air moving with the piston does not seem to contribute much to the piston impedance. The acoustic mass of the piston itself and its moving parts is a constant and the acoustic

mass of the air moving with the piston is very small in comparison to this and hence does not contribute to the acoustic mass of the piston. So M_{APair} can be neglected while evaluating the acoustic mass of the piston terms.

Figure 32 represents the frequency dependence of the acoustic resistance of the piston and all mechanical parts moving with the piston.

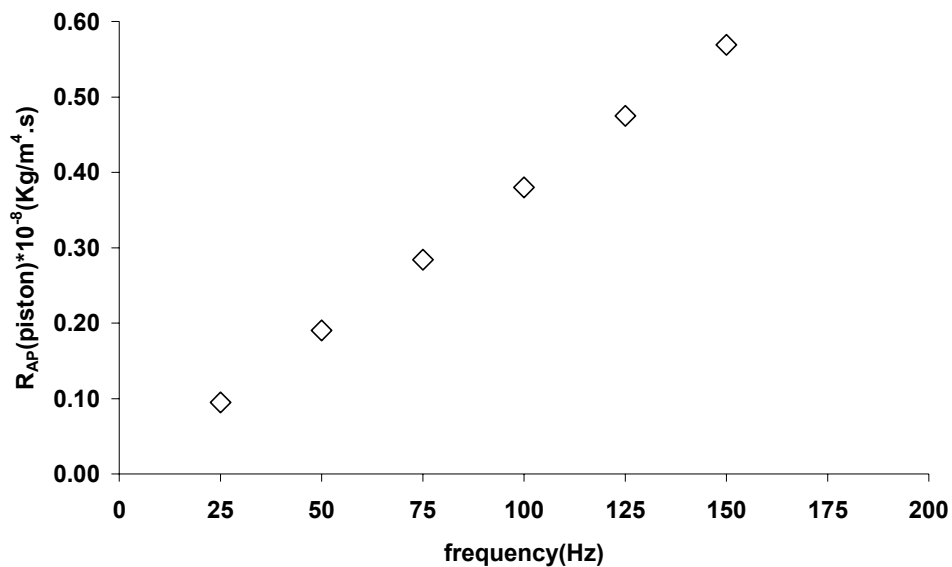


FIGURE 32. Frequency dependence of the acoustic resistance of mechanical parts moving with piston.

The acoustic resistance of the mechanical parts moving with the piston and the piston itself seems to vary linearly with motor frequency and contributes heavily to the piston impedance at higher frequencies.

Figure 33 represents the frequency dependence of the acoustic resistance of the air moving with the piston

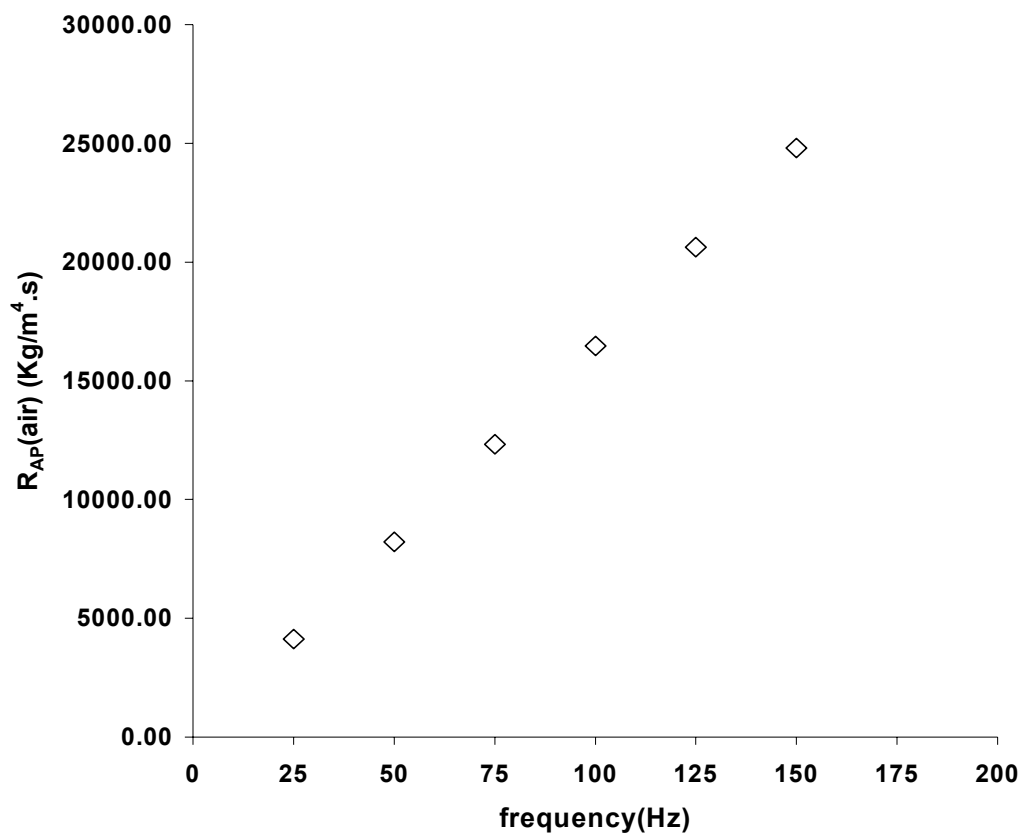


FIGURE 33. Frequency dependence of the acoustic resistance of air moving with piston.

The acoustic resistance of air moving with the piston also seems to vary linearly with motor driving frequency and though much smaller compared to the resistance of the mechanical parts of the piston, it still contributes to the impedance of the piston at higher

frequencies. At the frequencies tested however in our analysis, the acoustic resistance of the air moving with the piston is very small when compared to the acoustic resistance of the piston and its moving mechanical parts. Hence, the acoustic resistance of the air moving with the piston can be neglected while evaluating the acoustic resistance of the piston terms.

Figure 34 represents the frequency dependence of the acoustic mass of air in the exit slot neck.

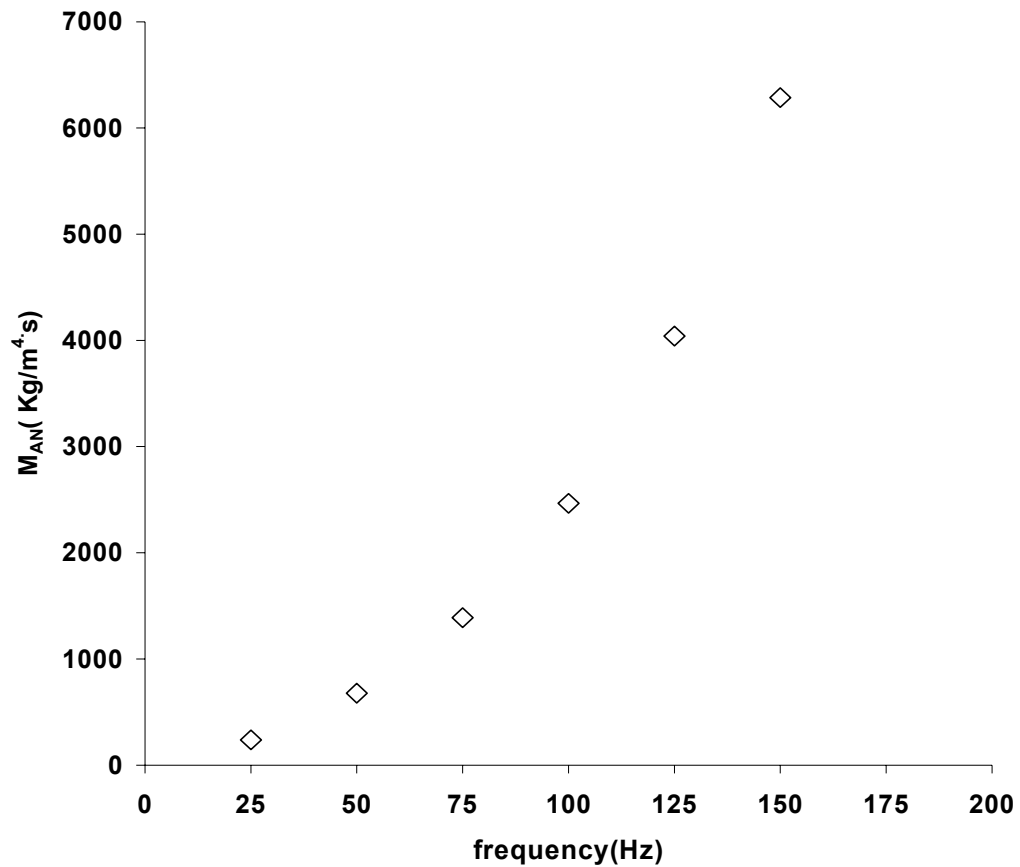


FIGURE 34. Frequency dependence of the acoustic mass of air in exit neck.

The acoustic mass of air in the exit slot seems to increase with the motor frequency as a polynomial function and at higher frequencies; it contributes heavily to the exit slot impedance term.

Figure 35 represents the frequency dependence of the viscous resistance of the air in the exit slot.

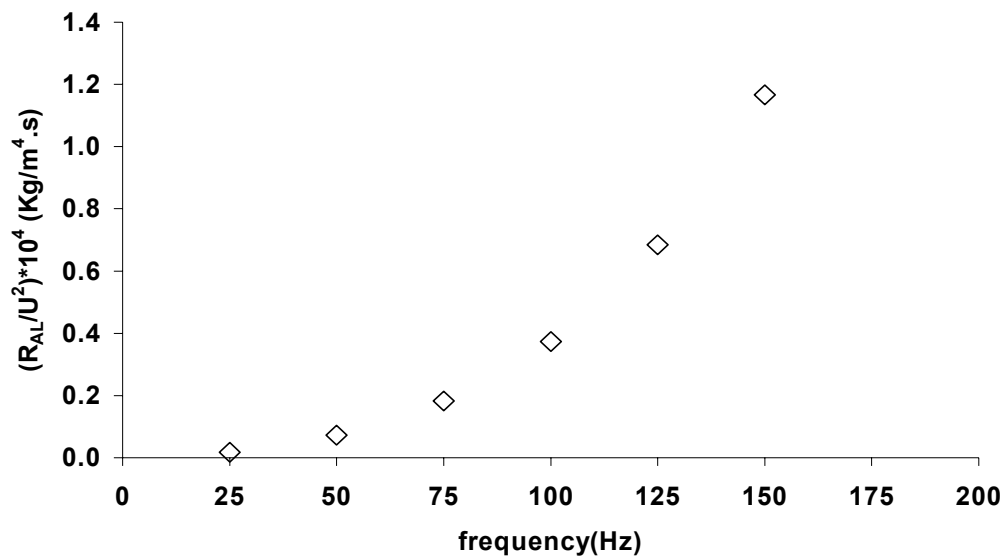


FIGURE 35. Frequency dependence of the viscous resistance of air in the exit neck.

The viscous resistance of the air in the exit slot also seems to vary as a cubic function of the motor frequency. Compared to the acoustic mass; however, it is very small. At higher frequencies; however, the viscous resistance contributes heavily to the exit slot impedance as expected.

Equations (51) and (65) are individually solved using a code written in Maple (Appendix C). The variation of the exit velocity with the motor operating frequency is

then studied using this model. Different slot widths are also tested to study the variation of the jet exit velocity with slot width. The cavity volumes currently tested do not show that much of a variation in the jet exit velocity using this model. The acceleration lengths of the exit slot are found to vary with slot width, with the smaller slot accelerating the jet faster and the larger slot accelerating it slower than the smaller slot. The results of this analysis are presented in the following section.

The electro-acoustic model is first compared with the theoretical incompressible jet exit velocity and the theoretical model developed in the previous chapter accounting for compressibility and viscous effects at the exit slot.

Figure 36 compares the electro-acoustic model jet exit velocity prediction and the incompressible and compressible cases at a slot width of 0.032 inches.

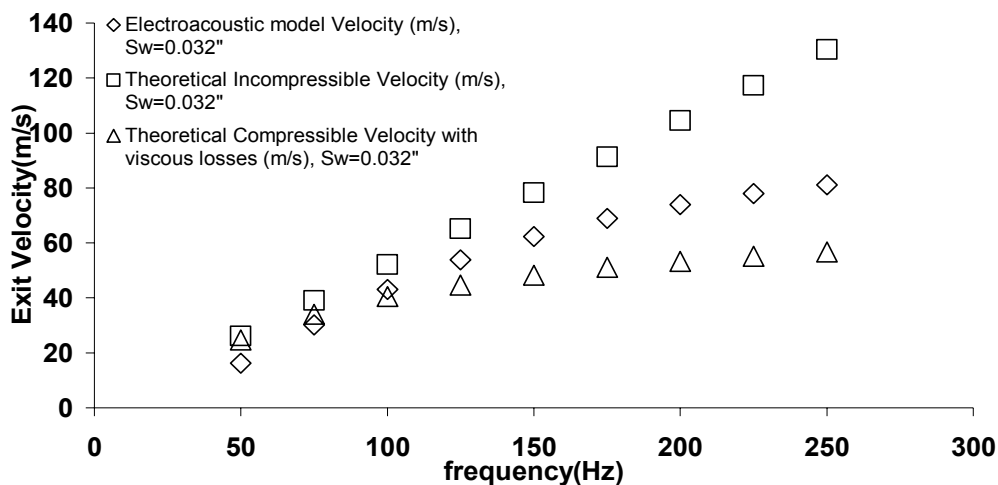


FIGURE 36. Comparison between electro-acoustic model and incompressible and compressible theoretical models at slot width 0.032".

From Figure 36, the electro-acoustic model matches with the incompressible case velocity at lower frequencies, as expected, and at higher frequencies, the compressibility effects dominate and hence the electro-acoustic model predicts velocities much less than the incompressible jet velocity. Also it is interesting to note that, the electro-acoustic model predicts jet velocities higher than the previously developed compressible model at higher frequencies, which should match the experimental velocities better. However, during the experimental studies, motor frequencies above 150 Hz could not be achieved and hence this conclusion could not be experimentally verified.

Figure 37 represents the comparison between the electro-acoustic model jet exit velocity prediction and the incompressible and compressible cases at a slot width of 0.064 inches.

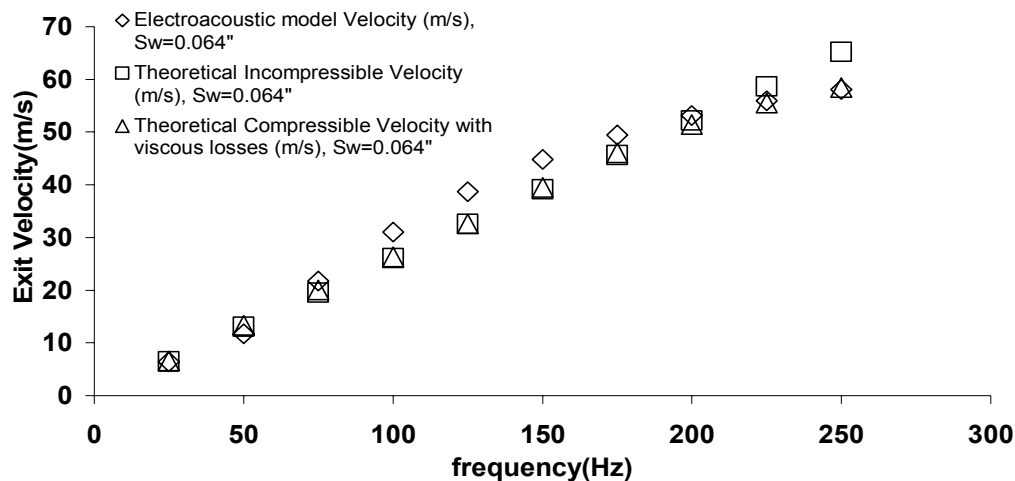


FIGURE 37. Comparison between electro-acoustic model and incompressible and compressible theoretical models at slot width 0.064".

From Figure 37, because the slot width is larger than the previous case, the compressibility effects do not predominate. The flow remains close to being

incompressible, even at high frequencies, and the deviation to compressibility seems to occur only at frequencies as high as 200 Hz. Even this deviation is very little compared to the effects shown at the smaller slot. This shows that the model predicts that smaller slots tend to be more compressible whereas larger slots behave more incompressible, even at higher frequencies. The electro-acoustic model predicts jet exit velocities slightly higher than the incompressible velocity at lower frequencies, which is not possible, and the cause of this deviation in the model needs to be studied and analyzed further.

The prediction of compressibility using this model is now summed up in Figure 38 which compares the incompressible and electro-acoustic model velocities for the small and large slot.

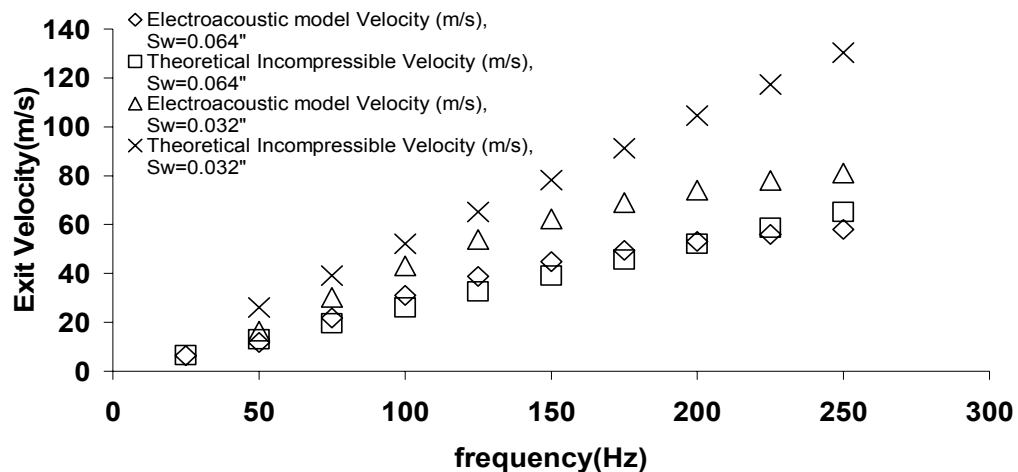


FIGURE 38. Compressibility prediction using electro-acoustic model for both large and small slot.

As stated previously, this plot shows that the electro-acoustic model predicts the dominance of compressibility at higher frequencies for the smaller slot and the flow being close to incompressible even at higher frequencies for the larger slot.

Figure 39 represents the variation of exit velocity with slot width predicted by the electro-acoustic model.

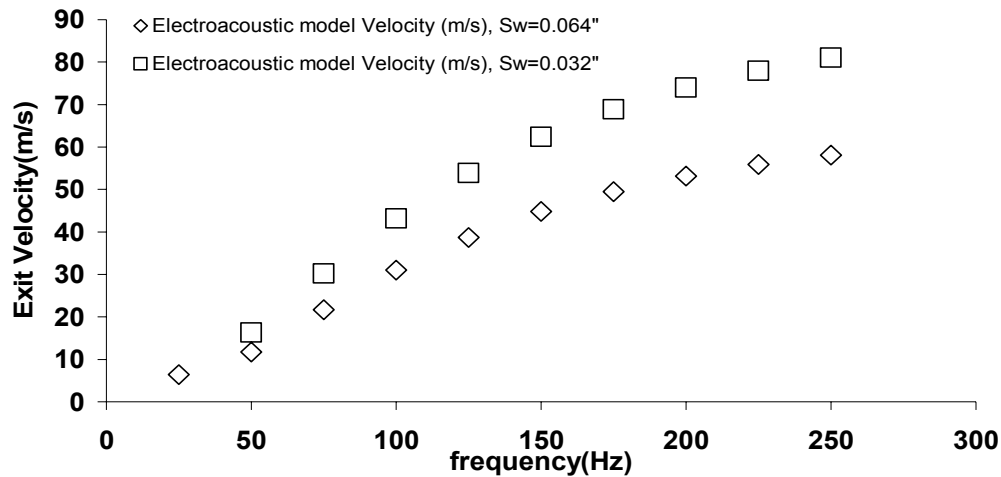


FIGURE 39. Variation of exit velocity with slot width using electro-acoustic model.

Based on Figure 39, the smaller slot produces larger velocities at all frequencies compared to the larger slot. The compressibility effects, as stated earlier dominate in the smaller slot at higher frequencies bringing down the velocities. The design of the exit slot needs to be optimized based on these plots to maximize the jet velocity to achieve more efficient flow reattachment and in the process also keeping the viscous and compressibility losses to a minimum.

The electro-acoustic model is validated by comparing the results of the model with experimental studies conducted using a hot wire anemometer under similar operating conditions.

Figure 40 compares the exit velocity prediction using the electro-acoustic model at a slot width of 0.032 inches with experimental studies at the same conditions.

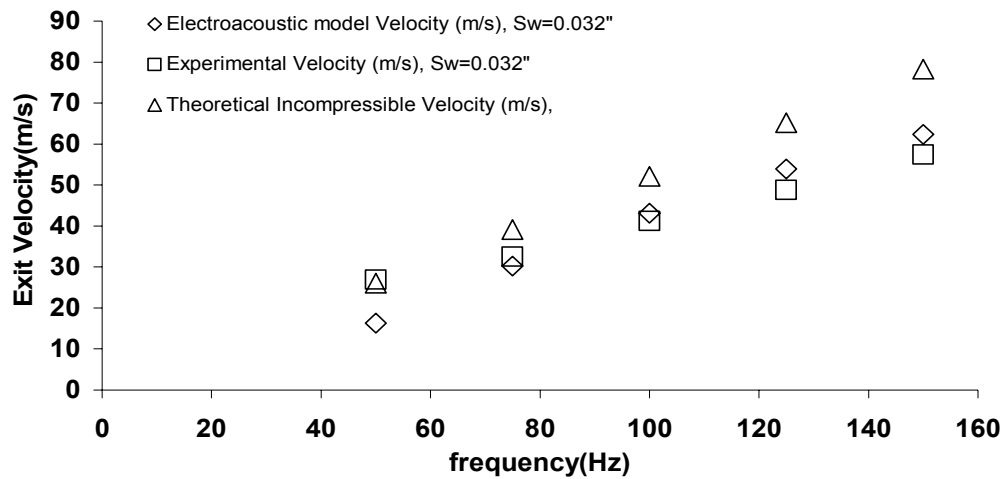


FIGURE 40. Comparison between electro-acoustic model prediction and experimental studies for slot width 0.032”.

Figure 40 shows that the electro-acoustic model predicts the jet exit velocity to an accuracy of 1 to 2 m/s at lower frequencies and at higher frequencies of about 100 to 150 Hz, the electro-acoustic model prediction is accurate to within 4 to 5 m/s. Considering the fact that actual values itself are of the order of 60 to 65 m/s at higher frequencies, the electro-acoustic model prediction error for the smaller slot is around 6%. The effect of compressibility and viscous losses at the exit in the experimental data at higher frequencies is also predicted well by the electro-acoustic model.

Figure 41 represents the comparison between the electro-acoustic model prediction and experimental studies for the larger slot (0.064 inches).

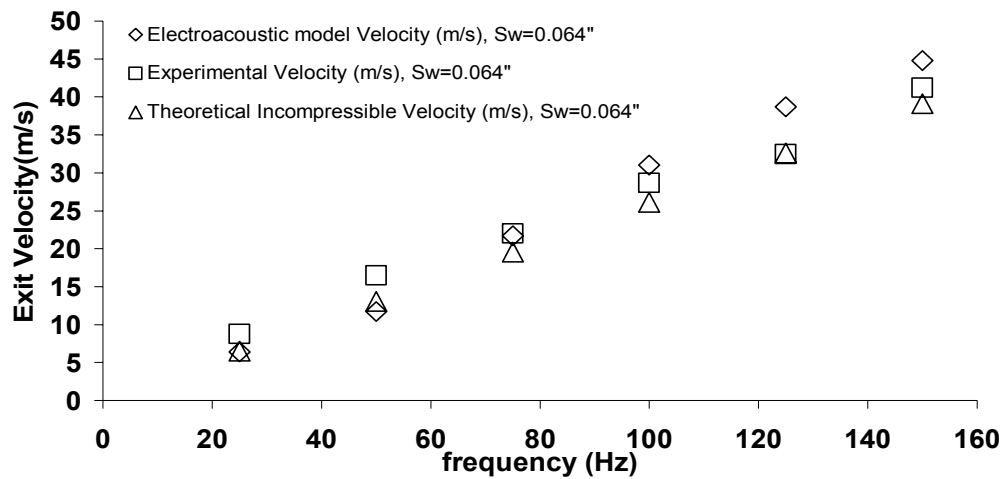


FIGURE 41. Comparison between electro-acoustic model prediction and experimental studies at 0.064" slot width.

The electro-acoustic model again predicts the exit slot velocity to an accuracy of 2 to 3 m/s for the larger slot, which is an error of 7 to 8 % at the velocities generated. As observed with the smaller slot, this prediction is much more accurate at lower frequencies and deviates slightly more at higher frequencies, where the flow is a little more compressible.

CONCLUSIONS

A dynamic electro-acoustic model to predict the frequency response function of the DC motor-driven synthetic jet actuator was presented. The effects of geometry and dimensions of the actuator parameters were analyzed using this model. The validity of the model was also tested by comparing the results with results of experimental study performed under similar operating conditions. Based on this comparison, at lower frequencies, the electro-acoustic model prediction has an error of 2 to 4% for both slots and at higher frequencies the model predicts the jet exit velocity with an error of 6 to 8% for both slots.

This model should help formulate feedback optimal control strategy for real time flow control using an array of actuators.

CONCLUSIONS

A theoretical model to predict the compressibility effects at the exit slot of a DC motor driven synthetic jet actuator for flow separation control was developed accounting for both viscous and inviscid flow conditions. The effects of geometry and material properties on the performance of the actuator were analyzed using these models. Based on the results of this analysis, the design of the SJA needs to be optimized to maximize flow reattachment. Comparing the results of the theoretical models with hot wire anemometer experimental studies conducted under similar conditions validated both of these models.

An electro-acoustic model to predict the frequency response function of the SJA was also developed. The effects of geometry and material properties are also studied using this model and as before the model results are validated by comparison with hot wire anemometer experimental studies. This model should enable optimal feedback control strategy for real time flow control using an array of actuators.

REFERENCES

- AMITAY, M., SMITH, B.L. AND GLEZER, A. 1998 Aerodynamic Flow Control Using Synthetic Jet Technology. *AIAA Paper* 98-0208, Reno, NV.
- CATTAFESTA, L., GALLAS, Q., MATHEW, J., KAYSAP, A., HOLMAN, R., NISHIDA, T., CARROLL, B. AND SHEPLAK, M. 2002 Lumped Element Modeling of Piezoelectric-Driven Synthetic Jet Actuators. *AIAA Paper* 2002-0215.
- CHEN, F.J., YAO, C., BEELER, G.B., BRYANT, R.G., AND FOX, R. L. 2000 Development of Synthetic Jet Actuators of Active Flow Control at NASA Langley. *AIAA Paper* 2000-2405.
- CROOK, A., SADRI, A.M. AND WOOD, N.J. 1999 The Development and Implementation of Synthetic Jets for the Control of Separated Flow. *AIAA Paper* 99-3176.
- CROOK, A. AND WOOD, N.J. 2001 Measurements and Visualizations of Synthetic Jets. *AIAA Paper* 2001-0145.
- FISCHER, F.A. 1955 *Fundamentals of Electroacoustics*, Interscience Publishers, Inc., New York.
- GAD-EL-HAK, M. AND BUSHNELL, D. 1991 Separation Control: Review. *ASME Journal of Fluids Engineering* **113**(3), 5-30.
- GREENBLATT, D. AND WYGNANSKI, I. 1998 Dynamic Stall Control by Oscillatory Forcing. *AIAA Paper* 98-0676.
- GILARRANZ, J.L. AND REDINIOTIS, O.K. 2001 Compact, High Power Synthetic Jet Actuators for Flow Separation Control. *AIAA Paper* 2001-0737, 39th Aerospace Sciences Meeting and Exhibit, Reno, NV.
- HUNT, F.V. 1982 *Electroacoustics: The Analysis of Transduction, and Its Historical Background*, 2nd Edition, Acoustical Society of America, Woodbury, NY.
- KRAL, L.D., DONOVAN, J.F., CAIN, A.B. AND CARY, A.W. 1997 Numerical Simulation of Synthetic Jet Actuators. *AIAA Paper* 97-1824.

- MALLINSON, S.G., REIZES, J.A., HONG, G. AND HAGA, H. 2000 The Operation and Application of Synthetic Jet Actuators. *AIAA Paper* 2000-2402.
- MCCORMICK, D. 2000 Boundary Layer Separation Control with Directed Synthetic Jets. *AIAA Paper* 2000-0519, 38th Aerospace Sciences Meeting and Exhibit, Reno, NV.
- MULLER, M.O., BERNAL, L.P., MORAN, R.P., WASSHABAUGH, P.D., PARVIZ, B.A. AND NAJAFI, K. 2000 Micromachined Acoustic Resonators for Microjet Propulsion. 38th Aerospace Sciences Meeting and Exhibit, Reno, NV, p. 3, eq. 2.
- RATHNASINGHAM, R. AND BREUER, K. 1997 Coupled Fluid-Structural Characteristics of Actuators for Flow Control. *AIAA Journal*, **35**, 832-837.
- RIZZETTA, D.P., VISBAL, M.R. AND STANEK, M.J. 1998 Numerical Investigation of Synthetic Jet Flowfields. *AIAA Paper* 98-2910.
- ROSSI, M. 1988 *Acoustics and Electroacoustics*, Artech House, Norwood, MA, pp. 245-373.
- SEIFERT, A. AND PACK, L. 1999 Oscillatory Excitation of Unsteady Compressible Flows Over Airfoils at Flight Reynolds Number. *AIAA Paper* 99-0925.
- SEIFERT, A., ELIAHU, S., GREENBLATT, D., WYGNANSKI, I. 1998 On the Use of Piezoelectric Actuators for Airfoil Separation Control. *AIAA Journal*, **36**, 1535-1537.
- SEIFERT, A., BACHAT, T., KOSS, D., SHEPSHELOVICH, M. AND WYGNANSKI, I. 1993 Oscillatory Blowing: A Tool to Delay Boundary-Layer Separation. *AIAA Journal*, **31**(11), 2052-2060.
- SEIFERT, A., DARABI, A. AND WYGNANSKI, I. 1996 On the Delay of Airfoil Stall by Periodic Excitation. *Journal of Aircraft*, **33**(4), 691-699.
- SMITH, D., AMITAY, M., KIBENS, V., PAREKH, D. AND GLEZER, A. 1998 Modifications of Lifting Body Aerodynamics Using Synthetic Jet Actuators. *AIAA Paper* 98-0209, 36th Aerospace Sciences Meeting and Exhibit, Reno, NV.

- UNO INGARD. 1953 On the Theory and Design of Acoustic Resonators. *The Journal of the Acoustical Society of America*, **25**, 762-789.
- WHITE, F.M. 1979 *Fluid Mechanics*, McGraw-Hill, Inc., New York.

APPENDIX A

Incompressible case

$$\text{str} := 0.811 \cdot 0.025^4$$

$$f := 200$$

$$T := \frac{1}{f}$$

$$h := 0.00001$$

$$n := 1..5 \cdot \frac{T}{h}$$

$$t_n := (n - 1) \cdot h$$

$$x_n := 0.5 \cdot \text{str} \cdot (1 - \cos(2 \cdot \pi \cdot f \cdot t_n))$$

$$\dot{x}_n := 0.5 \cdot \text{str} \cdot 2 \cdot \pi \cdot f \cdot \sin(2 \cdot \pi \cdot f \cdot t_n)$$

$$\text{pd} := 0.906 \cdot 0.025^4$$

$$A_p := \pi \cdot 0.25 \cdot \text{pd} \cdot \text{pd}$$

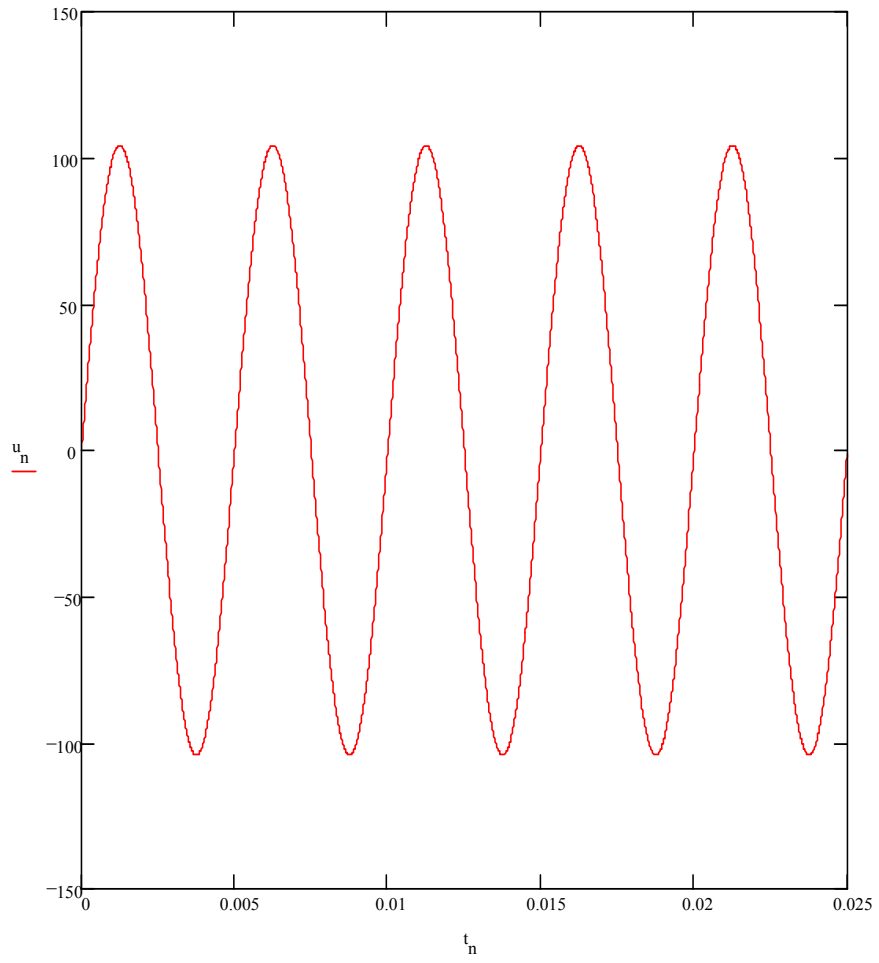
$$\text{sw} := 0.032 \cdot 0.025^4$$

$$\text{sl} := 2.5 \cdot 0.025^4$$

$$A_s := \text{sw} \cdot \text{sl}$$

$$u_n := \frac{A_p}{A_s} \cdot \dot{x}_n$$

$$f := 200 \text{ Hz}$$



APPENDIX B

Velocity at exit taking into account friction losses in throat and flow separation at exit plane

$f := 150$	frequency of oscillation
$T := \frac{1}{f}$	
$str := 0.811 \cdot 0.0254$	piston stroke
$hc := 0.3$	height of cavity
$sl := 2.5 \cdot 0.0254$	
$sw := 0.032 \cdot 0.0254$	
$lc := 2.5$	
$As := sw \cdot sl$	
$Vs := As \cdot 0.0254$	volume of slot
$wc := 1$	cav width
$Vc := wc \cdot lc \cdot hc \cdot 0.0254 \cdot 0.0254 \cdot 0.0254 + Vs$	volume of cavity
$pd := 0.906 \cdot 0.0254$	piston diameter
$Ap := \pi \cdot 0.25 \cdot pd \cdot pd$	area of piston
$sw := 0.032 \cdot 0.0254$	slot width
$sl := 2.5 \cdot 0.0254$	slot length
$L := 3 \cdot sw$	acceleration length
$ccl := 0.425 \cdot 0.0254$	
$pcv := (Ap \cdot ccl) + (Ap \cdot (str + 0.05 \cdot 0.0254))$	piston cylinder volume
$Vo := pcv + Vc$	total volume
$Vo = 2.719 \cdot 10^{-5}$	
$Vc = 1.36 \cdot 10^{-5}$	
$As := sw \cdot sl$	
$R := 287$	room temperature
$To := 299.4$	equivalent inertia length of exit throat
$Le := sl + \frac{(\pi \cdot As)^{0.5}}{4}$	

$L_v := 0.5 \cdot L_e$ equivalent viscous length of exit
 $h_t := s_w$ resonator throat height
 $\mu := 1.85 \cdot 10^{-5}$ viscosity of air
 $p_o := 1.013 \cdot 10^5$ atmospheric pressure
 $C_d := 0.4$ flow coefficient associated with streamline curvature at exit

plane

$$c := \frac{8 \cdot \mu \cdot L_v}{h_t^2 \cdot L_e}$$

$$c_4 := \frac{R \cdot T_o}{L_e}$$

$$c_3 := \frac{c \cdot R \cdot T_o}{p_o}$$

$$c_5 := \frac{1}{2 \cdot C_d^2 \cdot L_e}$$

$$h := 0.00001$$

$$n := 1..5 \cdot \frac{T}{h}$$

$$t_n := (n - 1) \cdot h$$

$$x_n := 0.5 \cdot \text{str} \cdot (1 - \cos(2 \cdot \pi \cdot f \cdot t_n))$$
 piston displacement

$$\dot{x}_n := 0.5 \cdot \text{str} \cdot 2 \cdot \pi \cdot f \cdot \sin(2 \cdot \pi \cdot f \cdot t_n)$$

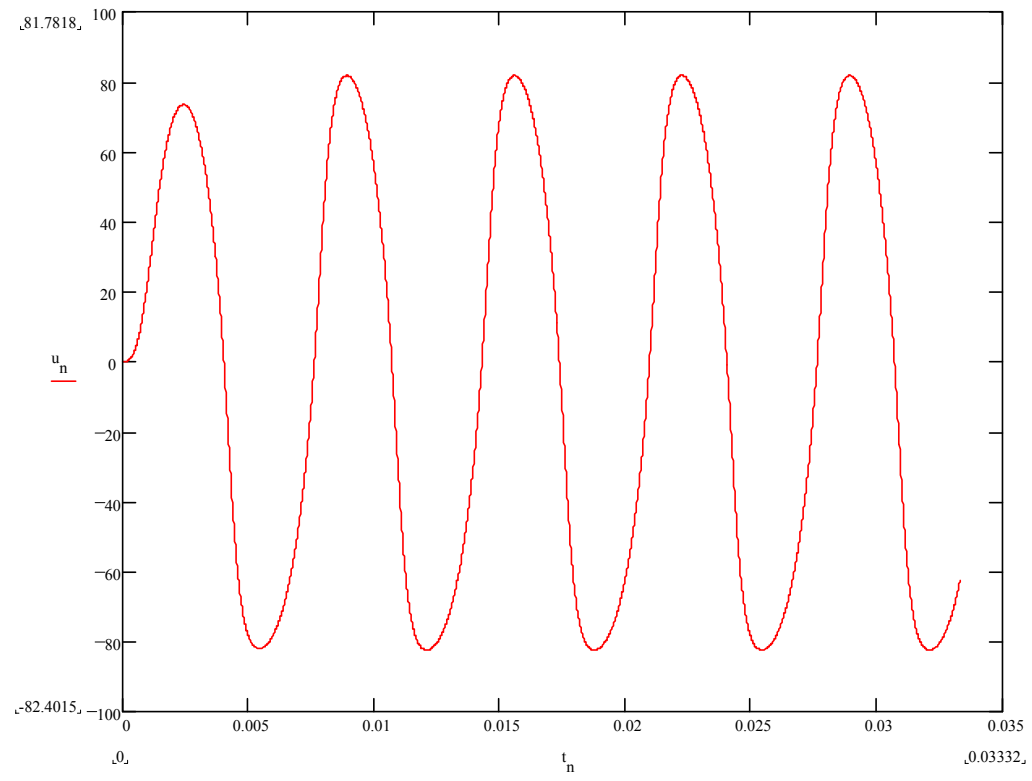
$$c_2_n := \frac{A_s}{(V_o - A_p \cdot x_n)}$$

$$c_1_n := \frac{A_p \cdot \dot{x}_n}{(V_o - A_p \cdot x_n)}$$

$$u_0 := 0$$

$$u_2 := u_1$$

$$u_{n+1} := \frac{u_n \cdot \left(\frac{2}{h^2} - c_4 \cdot c_2_n + c_1_n \cdot c_3 - c_2_n \cdot c_3 \cdot u_n \right) + u_{n-1} \cdot \left(c_5 \cdot \frac{|u_n|}{2 \cdot h} - \frac{1}{h^2} + \frac{c_3}{2 \cdot h} \right) + c_4 \cdot c_1_n}{\left(\frac{1}{h^2} + c_5 \cdot \frac{|u_n|}{2 \cdot h} + \frac{c_3}{2 \cdot h} \right)}$$



APPENDIX C

```

> # Common Variables for all impedances

> f:=250; # Frequency of oscillation of motor
      f:= 250

> rho:=1.225; # Density of air
      ρ := 1.225

> sw:=0.064*0.0254; # Width of exit slot
      sw := 0.0016256

> sl:=2.5*0.0254; # Length of exit slot
      sl:= 0.06350

> L:=0.9*sw; # Acceleration Length of air in exit slot
      L := 0.00146304

> An:=sw*sl; # Area of exit slot/neck
      An := 0.000103225600

> c:=340; # Speed of sound
      c := 340

> str:=0.811*0.0254; # Stroke of the piston
      str := 0.0205994

> pi:=22/7;
      π :=  $\frac{22}{7}$ 

> nu:=1.8*10^(-5); # Kinematic viscosity of air
      ν := 0.00001800000000

> mu:=nu*rho; # Dynamic Viscosity of air
      μ := 0.00002205000000

> omega:=2*pi*f; # Angular frequency of oscillation of motor
      ω :=  $\frac{11000}{7}$ 

> pd:=0.906*0.0254; # Piston diameter
      pd := 0.0230124

> Ap:=(pi*pd^2)/4; # Area of the piston
      Ap := 0.0004160911495

```



```

> ro:=pd/2; # Radius of piston head
      ro := 0.01150620000

> Up:=pi*f*str; # Amplitude of piston velocity
      Up := 16.18524286

> ws:=(omega*ro*ro)/nu; # Non-dimensional angular frequency
      ws := 11558.08748

> # Piston Impedance Terms

> # Map

> n:=20; #Number of points for numerical integration
      n := 20

> h:=pd/(2*n); #Interval width
      h := 0.0005753100000

> r[1]:=0;
      r1 := 0

> A:=(16*rho*str)/(Ap*Ap*ws*ws); #Amplitude of piston
velocity
      A := 0.01745668323

> integ[1]:=0; #Integrand to be evaluated for calculating
Map
      integ1 := 0

> for i from 2 by 1 to 21 do
> r[i]:=r[1]+(i-1)*h;
> rs[i]:=r[i]/ro;
> temp[i]:=sqrt(ws/2)*(1-rs[i]);
> temp1[i]:=(exp(-2*temp[i]))/rs[i];
> temp2[i]:=((2*exp(-temp[i]))*cos(temp[i]))/(sqrt(rs[i])));
> u[i]:=sqrt(1+temp1[i]-temp2[i]);
> integ[i]:=2*A*pi*r[i]*u[i]*u[i];
> end do;
>
Mapair:=(h/3)*(integ[1]+4*integ[2]+2*integ[3]+4*integ[4]+2*
integ[5]+4*integ[6]+2*integ[7]+4*integ[8]+2*integ[9]+4*inte
g[10]+2*integ[11]+4*integ[12]+2*integ[13]+4*integ[14]+2*int
eg[15]+4*integ[16]+2*integ[17]+4*integ[18]+2*integ[19]+4*in

```

```

teg[20]+integ[21]); #Acoustic mass of air moving with
piston
                                 $Mapair := 0.7055160443 \cdot 10^{-5}$ 

> Mp:=0.022; #Mass of piston and other moving parts of
piston
                                 $Mp := 0.022$ 

> Mappiston:=Mp/(Ap*Ap); #Acoustic mass of moving parts of
piston
                                 $Mappiston := 127070.7884$ 

> Maptot:=Mapair+Mappiston; #Acoustic mass of piston terms
                                 $Maptot := 127070.7884$ 

> # Rap

> n1:=20; #Number of points for numerical integration
                                 $n1 := 20$ 

> h1:=pd/(2*n1); #Interval width
                                 $h1 := 0.0005753100000$ 

> rr[1]:=0;
                                 $rr_1 := 0$ 

> G:=4*Up/ws;
                                 $G := 0.005601356760$ 

> ff[1]:=0; #Integrand to be evaluated for calculating Map
                                 $ff_1 := 0$ 

> for j from 2 by 1 to 21 do
> rr[j]:=rr[1]+(j-1)*h1;
> rss[j]:=rr[j]/ro;
> tem[j]:=sqrt(ws/2)*(1-rss[j]);
> tem1[j]:=exp(-2*tem[j])/rss[j];
> tem2[j]:=((2*exp(-tem[j]))*cos(tem[j]))/(sqrt(rss[j]));
> uu[j]:=sqrt(1+tem1[j]-tem2[j]);
> ff[j]:=2*G*pi*rr[j]*uu[j];
> end do;
>
Q:=(h1/3)*(ff[1]+4*ff[2]+2*ff[3]+4*ff[4]+2*ff[5]+4*ff[6]+2*
ff[7]+4*ff[8]+2*ff[9]+4*ff[10]+2*ff[11]+4*ff[12]+2*ff[13]+4
*ff[14]+2*ff[15]+4*ff[16]+2*ff[17]+4*ff[18]+2*ff[19]+4*ff[2
0]+ff[21]); #Flow rate of air moving with piston

```

```

Q := 0.2258344800 10-5

> Rapair := (8*mu*Up) / (pd*Q); #Acoustic resistance of air
moving with piston
Rapair := 54937.08819

> Mp := 0.022; #Mass of moving masses of piston
Mp := 0.022

> Rappiston := (2*Mp*pi*f) / (Ap*Ap); #Acoustic resistance of
moving mass of piston (mechanics)
Rappiston := 0.1996826674 109

> Rap := Rapair + Rappiston; #Acoustic resistance of piston
terms
Rap := 0.1997376045 109

> # Cavity Impedance Terms

> # Cac

> hc := 0.3*0.0254; #Height of cavity
hc := 0.00762

> wc := 1*0.0254; #Width of cavity
wc := 0.0254

> lc := 2.5*0.0254; #Length of cavity
lc := 0.06350

> Vc := hc*lc*wc; #Volume of cavity
Vc := 0.00001229029800

> Cac := (Vc) / (rho*c*c); #Acoustic compliance of cavity
Cac := 0.8678976064 10-10

> # Exit Slot Impedance Terms

> # Can

> Vn := An*L; #Volume of exit slot neck
Vn := 0.1510231818 10-6

> Can := (Vn) / (rho*c*c); #Acoustic compliance of air in the
exit slot
Can := 0.1066472578 10-11

```

```

> # Man

> m1:=((rho*L*s1)/(An*An))*sqrt((2*nu)/(omega));
      m1 := 1.616572215

> m2:=(sw/2)*sqrt((omega)/(2*nu));
      m2 := 5.370067775

> Man:=m1*(2*m2+sinh(2*m2)-2*sinh(m2)*cos(m2)-
2*cosh(m2)*sin(m2)); #Acoustic mass of air in the neck
      Man := 37400.38104

> Kd:=0.75; # Jet dump loss coefficient associated with exit
slot discharge
      Kd := 0.75

> Ran:=(0.5*Kd*rho*U)/(An); #Acoustic resistance of neck
accounting for jet dump loss
      Ran := 4450.204213 U

> # Ral

> Rs:=sqrt(mu*rho*omega/2); # Surface resistance of air at
exit slot of rectangular slot
      Rs := 0.1456815877

> r1:=(Rs*U*U*s1/2)*sqrt(2*nu/omega);
      r1 := 0.7000875000 10-6 U2

> r2:=(sw/2)*sqrt((omega)/(2*nu));
      r2 := 5.370067775

> Ral:=r1*(2*r2+sinh(2*r2)-2*sinh(r2)*cos(r2)-
2*cosh(r2)*sin(r2)); #Acoustic resistance of air in the
neck accounting for viscous effects
      Ral := 0.01619694995 U2

> # Evaluation of frequency response function from motor
dynamics

> Vs:=0.0006*f*f+0.0429*f+5.4; #Supply voltage of motor
      Vs := 53.6250

> Kt:=7.13*10(-4); #Torque constant of motor
      Kt := 0.0007130000000

> Rm:=0.041; #Winding resistance of armature of motor

```

```

Rm := 0.041

> Pl:=(2*pi*Kt*Vs*f) / (Rm) - (4*pi*pi*Kt*Kt*f*f) / (Rm); #Useful
load power of motor
Pl := 1434.820048

> Ptot:=Pl/0.8; #Total power delivered by motor
Ptot := 1793.525060

> po:=1.013*10^(5); # Standard Atmospheric pressure
po := 101300.000

> # phi:=(po+1/2*rho*(U*U-pi*pi*f*f*str*str)) / (Vs); #Turns
ratio to convert acoustic to electric domain
> Qp:=Up*Ap; phi:=10^(8); #Flow rate of air moving with
piston
Qp := 0.006734536307
phi := 100000000

> Vac:=Ptot / (Vs/Rm); #Dummy voltage for electroacoustic
circuit
Vac := 1.371273239

> Qout:=U*An; #Volumetric flow rate of air through the exit
slot
Qout := 0.000103225600 U

> frfmotor:=Qout/Vac; #Frequency response function
frfmotor := 0.00007527719280 U

> # Evaluation of frequency response function from electro-
acoustic circuit

> A1:=Can*(Rap+Ran+Ral)+Cac*Rap;
A1 := 0.01754819357 + 0.4746020760 10-8 U + 0.1727360297 10-13 U2

> A2:=Cac*Can*Rap*(Ran+Ral)+Can*(Maptot+Man)+Cac*Maptot;
A2 := 0.8227311888 10-10 U + 0.2994409975 10-15 U2 + 0.00001120384730

```

```

> A3:=Cac*Can*(Rap*Man+Maptot*Ran+Maptot*Ral);
   $A3 := 0.6914392795 \cdot 10^{-9} + 0.5234122089 \cdot 10^{-13} U + 0.1905009511 \cdot 10^{-18} U^2$ 

> A4:=Cac*Can*Maptot*Man;
   $A4 := 0.4398857923 \cdot 10^{-12}$ 

frfcircuit:=(phi*Can*f)/(1+A1*f+A2*f*f+A3*f*f*f+A4*f*f*f*f)
;
   $frfcircuit :=$ 
  
$$0.02666181445 \frac{1}{6.099810891 + 0.7146406696 \cdot 10^{-5} U + 0.2601004044 \cdot 10^{-10} U^2}$$


> # Evaluation of exit velocity from final equation

> exit_eqn:=frfcircuit-frfmotor=0;
   $exit\_eqn :=$ 
  
$$0.02666181445 \frac{1}{6.099810891 + 0.7146406696 \cdot 10^{-5} U + 0.2601004044 \cdot 10^{-10} U^2}$$

  
$$- 0.00007527719280 U = 0$$


> solve(exit_eqn,U);
   $-137406.8769 - 464384.3810 I, -137406.8769 + 464384.3810 I, 58.06044611$ 

```

VITA

Name	Ashwin Kumar Balasubramanian
Permanent Address	4405, Aspen Street, Apt #C, Bryan, Texas – 77801, USA
Educational Background	M.S., Texas A&M University, College Station, USA. Major Subject: Aerospace Engineering Graduation Date: August 2003 B.Tech, Indian Institute of Technology, Madras, India Major Subject: Ocean Engineering Graduation Date: May 2000
Professional Experience	Graduate Research Assistant at Fluid Dynamics Lab (01/01-present) Designed a D/C motor driven synthetic jet actuator for flow separation control and studied its compressibility effects using a theoretical model. Also developed an electro-acoustic model to predict the frequency response of the actuator and the performance of the actuator under different conditions. Graduate Teaching Assistant at Texas A&M University (01/02-05/03) Teaching assistant for Aircraft Vehicle Design class. Helping students build a wind tunnel test model using a rapid prototype machine and based on these results, a radio controlled model is built and tested at the flight mechanics lab.
Publications	“Biomimetic nano-structure skin for hydrodynamic drag reduction”, paper published in AIAA conference proceedings and presented at the AIAA Micro Fluidics Conference, Reno, Nevada in January 2003.